5 Hadronic calorimetry

The hadronic calorimetry of ATLAS (a view of which is presented in Figure 1-iii) consists of three main devices. In the barrel region ($|\eta| < 1.7$) there is the scintillating Tile Calorimeter. The Hadronic End-cap LAr Calorimeter (HEC) extends up to $|\eta| = 3.2$. The range $3.1 < |\eta| < 4.9$ is covered by the high density Forward Calorimeter (FCAL). Up to $|\eta| = 2.5$ the basic granularity of the hadron calorimeters is $\Delta\eta \times \Delta\phi = 0.1 \times 0.1$. This region is to be used for precise measurements of the energy and angles of jets and, at low luminosity, of single charged particles. In the region $|\eta| > 2.5$, the basic granularity is approximately $\Delta\eta \times \Delta\phi = 0.2 \times 0.2$. A more detailed description of all ATLAS calorimeters is given in the Calorimeter TDRs ([5-1], [5-2], [5-3]) and in Section 1.5 of this document.

Recent test beam results from prototypes and module zero's of these detectors are presented in Section 5.1 to illustrate their basic performance. They are compared with predictions of the hadronic shower simulation package used for the studies presented in this report. In Section 5.2 the changes in the overall design of the ATLAS calorimetry since the Calorimeter TDRs are reviewed. The performance of the calorimetry for single particle detection for the full pseudorapidity range is described in Section 5.3 (performance for jets and for missing E_T measurements is described in Chapter 9). In Section 5.4 the possibility of calibrating the calorimeters with single charged hadrons is discussed.

5.1 Test beam results for pions, muons and electrons

The performance for single particle detection, obtained from recent test beam results, is reviewed in this section. Results are presented for the three main sections of the calorimetry: the barrel, end-cap and forward calorimeters.

5.1.1 Combined tests of the EM LAr and Hadronic Tile Calorimeters

Combined tests of the EM LAr and Tile barrel calorimeter prototypes have been performed in 1994 [5-4] and 1996 [5-5] with a set-up representative of the final configuration. The LAr and Tile prototype modules used in the test beam have performances similar to the final modules. The cryostat dead material and the distance between the two prototypes were close to the actual set-up. One difference was that the Tile prototypes were 1.80 m long and segmented in four longitudinal compartments, while the final modules are 1.60 m thick and have three compartments in depth. A presampler in front of the LAr barrel prototype was used to select minimum ionising particles and thus to remove particles with early interactions which could take place in the material in front of the calorimeter.

The simplest method to reconstruct the pion energy, denoted as the 'Benchmark Method', consists of introducing a set of energy independent corrections. Both prototypes were first calibrated at the electromagnetic scale. The total reconstructed energy is then expressed as:

$$E_{rec} = a \cdot E_{had} + E_{em} + b \cdot E_{em}^{\,2} + c \cdot \sqrt{a \cdot E_{had1} \cdot E_{em3}} \; . \qquad \text{5-1}$$

Both calorimeter sections are non-compensating and the coefficient a takes into account their different responses to the pion energy. The quadratic term $bE_{em}^{\,2}$ provides a first order correction for the non-compensation (the coefficient is negative, it suppresses the signal for events with a
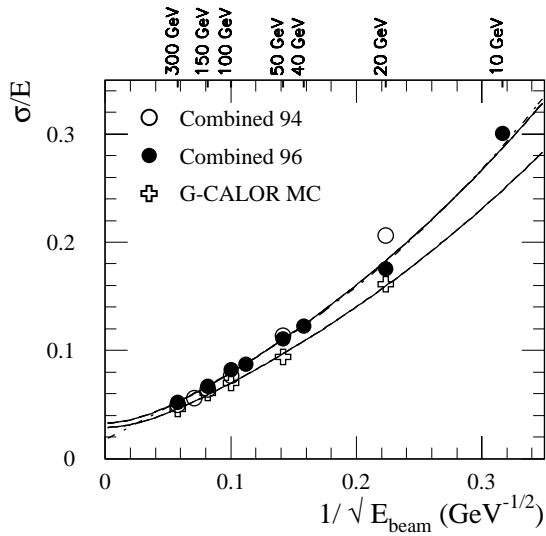
Figure 5-1 Energy resolution for pions as obtained with the Benchmark Method. The solid dots (open circles) give the results for the 1996 (1994) test beam data, the crosses show the G-CALOR predictions. The solid lines give fits with Equation 5-3, the dashed-dotted line gives a fit with Equation 5-2.
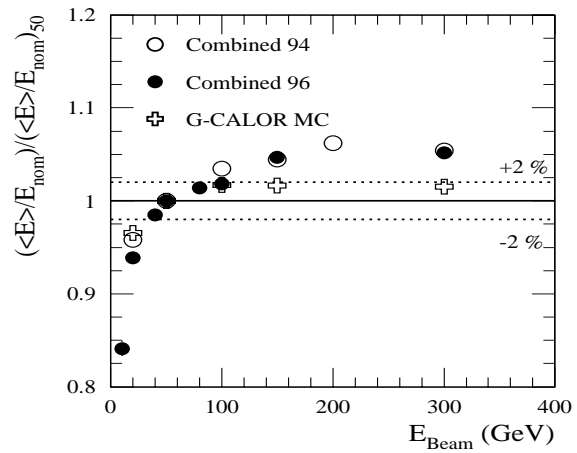
Figure 5-2 Relative non-linearity as a function of the beam energy for the Benchmark Method. The solid dots (open circles) give the results for the 1996 (1994) test beam data, the crosses show the G-CALOR predictions. The points are normalised to the 50 GeV case.

large fraction of electromagnetic energy). The last term estimates the energy loss in the cryostat wall separating the two calorimeters. The validity of using the geometric mean of the last LAr compartment energy (E_{em3}) and the first Tile Calorimeter compartment energy (E_{had1}) has been tested with the insertion of a mid-sampler between the calorimeters. The values of the coefficients are obtained by minimising the energy resolution for 300 GeV pions. The resolution for pions obtained with the Benchmark Method is shown in Figure 5-1. The energy dependence of the resolution can be parametrised by one of the following formulae:

$$\sigma/E = (A/\sqrt{E} + B) \oplus C/E , \qquad\qquad 5\text{-}2$$

$$\sigma/E = A/\sqrt{E} \oplus B \oplus C/E , \qquad\qquad 5\text{-}3$$

where the resolution σ/E is usually in percent, the sampling term A is in % GeV$^{1/2}$, the constant term B is in percent and the noise term C is in GeV. Results of the fit with these expressions are given in Table 5-1. The results are compared to the prediction of the G-CALOR hadronic shower simulation package [5-6].

Table 5-1 Terms of the pion energy resolution as obtained with the Benchmark Method.

	A (% GeV$^{1/2}$)	B (%)	C (GeV)
Experimental data: Equation 5-2 fit	59.5 ± 0.3	1.8 ± 0.2	2.0 ± 0.1
Experimental data: Equation 5-3 fit	69.8 ± 0.2	3.3 ± 0.2	1.8 ± 0.1
G-CALOR prediction: Equation 5-3 fit	61.7 ± 0.1	2.9 ± 0.3	fixed at 1.5

With the simple Benchmark Method, the effect of non-compensation is not fully corrected for and the pion response shows some non-linearity (see Figure 5-2), of the order of 5% in the range between 50 and 300 GeV. G-CALOR predicts only 2% of non-linearity of the response in the same energy range.

The degree of non-compensation of the calorimeter *e/h*, that is the ratio of the calorimeter response to the electromagnetic and non-electromagnetic (purely hadronic) component of the hadron showers, can be determined from the energy dependence of the *e/π* ratio. This ratio depends on *e/h* and on the electromagnetic fraction $F(\pi^0)$ produced in the interaction:

$$e/\pi = \frac{e/h}{1 + (e/h - 1) \cdot F(\pi^0)}. \qquad \text{5-4}$$

To extract the value of *e/h*, the pion response has to be calculated using the electromagnetic scale only, hence Equation 5-1 becomes simply

$$E_{rec} = E_{em} + E_{had} + E_{cryo}$$

and the fraction of π^0's is taken as $F(\pi^0) = 0.11 \cdot \ln E$ [5-7]. The fit results in a value of *e/h* of the order of 1.35-1.37 (see Figure 5-3). G-CALOR again predicts a lower level of non-compensation.

Figure 5-3 Energy dependence of the *e/π* ratio, fitted with Equation 5-4. The solid dots (open circles) give the results for the 1996 (1994) test beam data, the crosses show the G-CALOR predictions.

A second method to correct for the effect of non-compensation was applied to the data. This weighting technique, inspired on a method developed for the LAr calorimeters of the H1 experiment at HERA [5-8], consists of correcting upwards the response of individual cells with relatively small signals, to equalise their response to that of cells with large (typically electromagnetic) deposited energies. The reconstructed energy is expressed as

$$E_{rec} = \sum_{em-cells} (W_{em}(E_{cell}) \cdot E_{cell}) + \sum_{had-cells} (W_{had}(E_{cell}) \cdot E_{cell}) + E_c.$$

The weights are characteristic parameters of the calorimeter type, the electromagnetic (*em*) or hadronic (*had*) compartments, and they vary smoothly with the energy of the incident particle. The energy resolution obtained with this method is shown in Figure 5-4 (see also Table 5-2) and the relative response as a function of the energy is shown in Figure 5-5. The resolution is improved and the linearity restored to better than 2%.

5.1.2 Tile Calorimeter module zero test beam results

An extensive test beam programme of the Tile Calorimeter barrel and extended barrel module zero's has been carried out starting in 1996. The response to charged pions, electrons and muons has been studied.
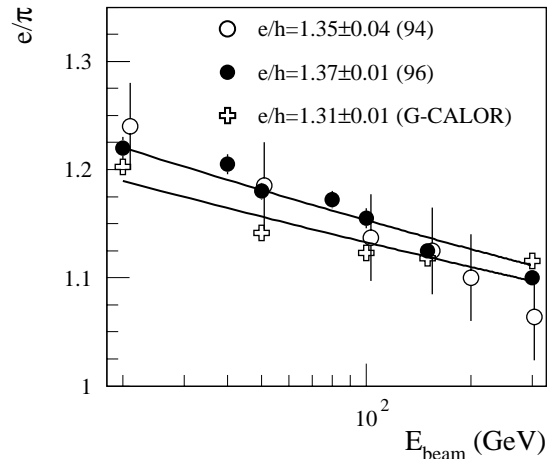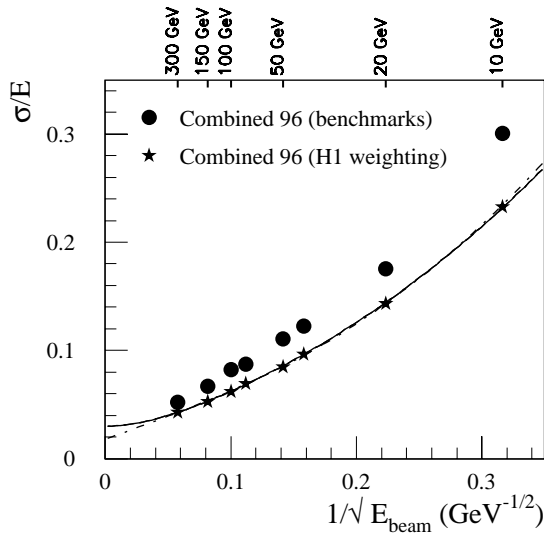
Figure 5-4 Energy dependence of the energy resolution for pions as obtained with the H1 cell-weighting method. The solid line is a fit with Equation 5-3, the dashed-dotted line is a fit with Equation 5-2.
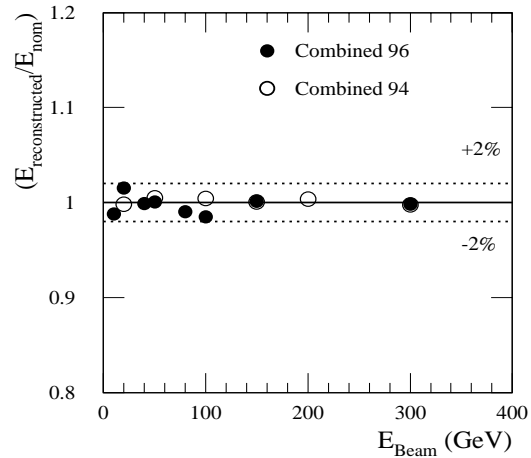
Figure 5-5 Energy dependence of the relative non-linearity for pions as obtained with the H1 cell-weighting method.

Table 5-2 Terms of the pion energy resolution as obtained with the H1 cell-weighting method.

	A (% GeV$^{1/2}$)	B (%)	C (GeV)
Experimental data: Equation 5-2 fit	41.9 ± 0.2	1.8 ± 0.1	1.8 ± 0.1
Experimental data: Equation 5-3 fit	52.1 ± 0.1	3.0 ± 0.1	1.6 ± 0.1

Table 5-3 Terms of the pion energy resolution for the module zero of the Tile Calorimeter.

	A (% GeV$^{1/2}$)	B (%)
Experimental data: Equation 5-2 fit	43.6 ± 0.8	2.4 ± 0.1
G-CALOR prediction: Equation 5-2 fit	42.6 ± 0.2	1.7 ± 0.2
Experimental data: Equation 5-3 fit	52.0 ± 0.6	4.1 ± 0.1
G-CALOR prediction: Equation 5-3 fit	48.0 ± 1.2	3.3 ± 0.2

5.1.2.1 Response to pions

The response of the detector to pions has been measured in the energy range from 10 to 400 GeV. Figure 5-6 shows the energy resolution obtained in the barrel module zero for pions, when summing the total energy deposited in the calorimeter without any correction for non-compensation. The hadronic shower was required to start in the first compartment to avoid longitudinal leakage, since the thickness of the module (1.60 m) was adapted to the final configuration, *i.e.* with the additional 1.2 λ of the LAr calorimeter in front. The data are in good agreement with the results obtained with the 1.80 m thick Tile Calorimeter prototype. The resolution is well fitted with the formulae in Equation 5-2 and Equation 5-3 with the term $C = 0$, since the noise contribution is negligible (see Table 5-3). The e/π ratio is shown in Figure 5-7. The fitted level of non-compensation of the calorimeter is $e/h = 1.30 \pm 0.01$. The G-CALOR Monte Carlo predicts (see Table 5-3) a similar sampling term, as for the experimental data, but a small-
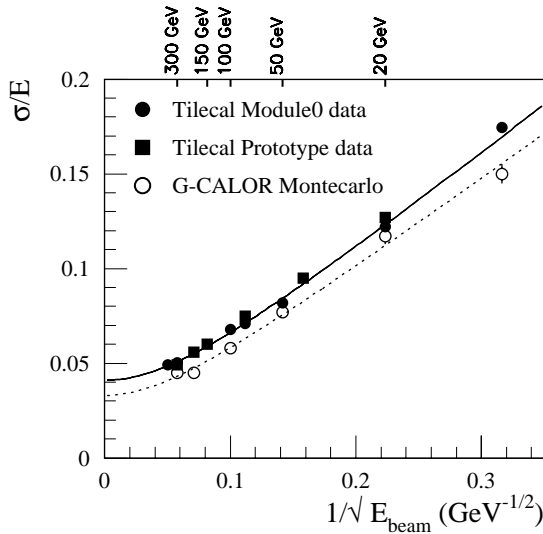
Figure 5-6 Energy resolution for pions, measured in the Tile Calorimeter barrel modules for incident pion energies between 10 and 400 GeV. The lines give fits with Equation 5-3.
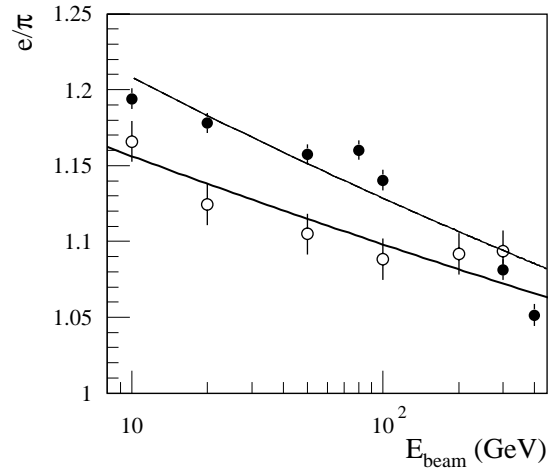

Figure 5-7 e/π ratio measured in the Tile Calorimeter barrel module zero for incident pion energies between 10 and 400 GeV. The solid dots show experimental data, the open circles show G-CALOR prediction. The dependencies are fitted with Equation 5-4.

er constant term and a lower level of non-compensation of $e/h = 1.22 \pm 0.02$ [5-9]. A good uniformity of the response of the module as a function of pseudorapidity and azimuthal angle was observed [5-3].

5.1.2.2 Response to electrons

The electron response for the module zero of the Tile Calorimeter was measured in the energy range from 10 to 300 GeV [5-10]. The electrons were sent at 90° with respect to the planes of scintillator tiles. The energy dependence of the resolution is shown in Figure 5-8. The energy resolution is well fitted with the modified square sum formula without the noise term:

$$\sigma/E = A/\sqrt{E} \oplus B .$$
  5-5

The sampling term A of the energy resolution is $(25.6 \pm 0.4)\%$ GeV$^{1/2}$ and the constant term B is $(0.67 \pm 0.04)\%$.

5.1.2.3 Response to muons

The response to muons was extensively studied in the Tile Calorimeter test beam programme. In particular, the response in the
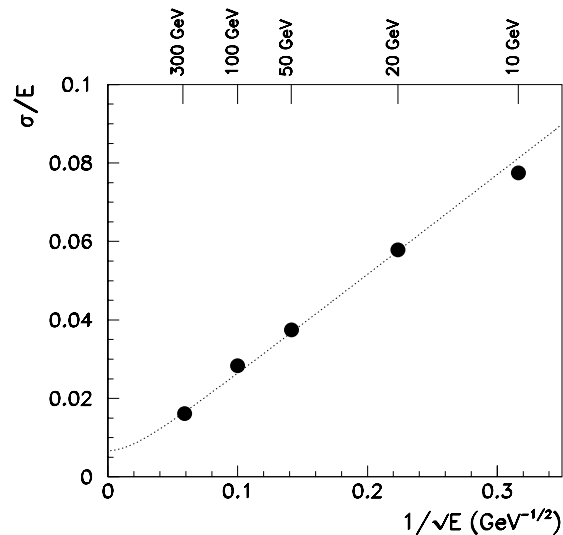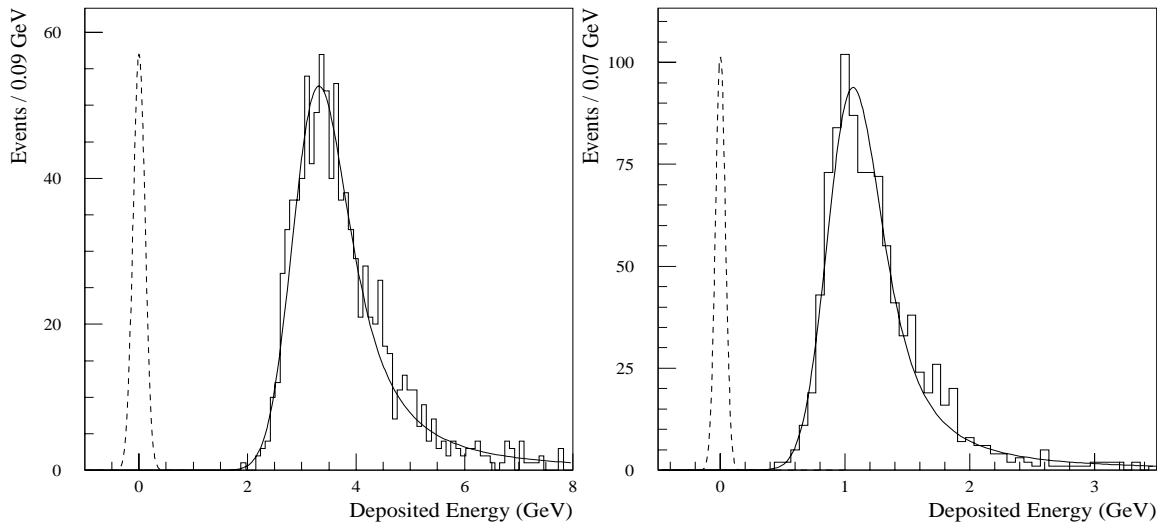

Figure 5-8 Energy dependence of the energy resolution for electrons, measured in the Tile Calorimeter barrel module zero. The line is a fit with Equation 5-5.

Figure 5-9 Total deposited energy (left-hand plot) and energy deposited in the third compartment (right-hand plot) by 100 GeV muons in the Tile Calorimeter extended barrel module zero at a pseudorapidity of 1.3. The signal is fitted with a Landau distribution convoluted with a Gaussian. The peaks around zero (dashed) are the electronic noise distributions.

three compartments of the calorimeter as a function of pseudorapidity was measured. The ability to measure a clean signal above noise allows the Tile Calorimeter to contribute to the muon identification at the trigger and analysis levels. An example of the total signal deposited by 100 GeV muons in the full Tile Calorimeter is given in Figure 5-9 (left-hand plot). The signal is fitted with the convolution of a Landau distribution with a Gaussian [5-11]. The peak, or most probable value, is at 3.32 GeV. The FWHM is 1.3 GeV. The signal is asymmetric; the left-hand side of the peak is essentially a Gaussian with $\sigma = 0.48$ GeV. Typically the signal has to be summed over three to four cells, or six to eight photomultiplier tubes (PMT). The expected level of electronic noise is about 20 MeV per PMT, hence about 55 MeV for eight PMTs. In the test beam, some channels were equipped with different electronics. The actual noise level (see dashed distribution in the left-hand plot of Figure 5-9) was 100 MeV, dominated by the contribution of the two PMTs of the first compartment. The signal is separated by more than six standard deviations from the noise.

Since in physics events muons may overlap with other particles and, at high luminosity, minimum bias events may deposit a non-negligible amount of energy in the innermost layers of the calorimeter, the ability to see a clean muon signal in the outermost compartment is an important asset. The right-hand plot of Figure 5-9 shows the signal deposited by muons in the third compartment. The peak is at 1.06 GeV and the FWHM is 0.55 GeV. The left-hand side of the peak is essentially a Gaussian with $\sigma = 0.20$ GeV. The electronic noise contribution from summing the signal of two PMTs (shown as a dashed distribution on the right-hand plot) is 40 MeV. The signal is separated from the noise by five standard deviations. More experimental information about the response of the muons in the Tile Calorimeter (barrel and extended barrel) modules can be found in Section 5.3.3.

5.1.3 Hadronic end-cap calorimeter module zero test beam results

5.1.3.1 The test beam set-up

Beam tests of Hadronic End-cap Calorimeter (HEC) module zero's have been performed in the H6 beam line of the CERN SPS. Four modules, two of the front wheel and two of the rear wheel, have been exposed in 1998 to electron, pion and muon beams at energies in the range 10-200 GeV.

In contrast to the final detector configuration, the impact angle of the beam with respect to the calorimeter front face was chosen to be 90°, irrespective of the impact position. Thus lateral energy leakage could be minimised - an important issue given the limited lateral coverage of the two ϕ-wedges of the total wheel used. Impact positions were typically within ±25 cm of the centre of the modules in the vertical and horizontal directions. This allowed detailed measurements to be made of the homogeneity of the response for electrons, pions and muons. In particular, the response when crossing the inactive regions (*e.g.* the crack between the modules) was studied in detail. In addition, energy scans in up to 16 different impact positions were carried out and yielded detailed information on the expected performance of the calorimeter. The data were analysed using the standard digital filtering technique and signal reconstruction [5-12].

5.1.3.2 Noise performance

The noise measured for an individual channel was typically 290 (400, 800) MeV for the first (second, third) longitudinal compartment. These results were obtained using a digital filtering technique with five time samplings [5-13]. Digital filtering reduced the noise by a factor of order 1.5. As expected, the noise per channel was correlated with the related read-out cell capacitance. In addition, some coherent noise was present, typically at the level of 20%. The source of this coherent noise was traced back to the shaper and preshaper card. This part of the read-out electronics is being redesigned.

5.1.3.3 Results for electrons

The electron signal was reconstructed from a cluster of the most active read-out cells. The clusters use typically from three to seven cells, all located in the first two longitudinal compartments, *i.e.* in the first wheel only ([5-14], [5-15]). Using all data sets, an overall calibration constant (from nA to GeV) was determined from a χ^2-minimisation of the energy resolution. The energy resolution was parametrised using Equation 5-3, where the term *C* reflects the electronic noise. The noise was determined from the read-out cells of the related cluster for the given impact point using randomly triggered events or from a three parameter fit to the energy resolution.

The parameters *A*, *B* and *C* were obtained from a fit to the data of each individual impact point. For four different impact positions, the results are shown in Figure 5-10. In this figure, the energy resolution as a function of the electron energy is shown along with the result of the fit (solid line). Typical values obtained for the sampling and constant terms were $A = (21.0 \pm 0.5)\%\ \text{GeV}^{1/2}$ and $B = (0.2 \pm 0.2)\%$. These results agree well with Monte Carlo expectations. The noise term was determined to be 0.7-1.0 GeV. Reducing the cluster size to three cells changed the noise to the level of 0.5 GeV with an energy resolution only marginally worse. The linearity of the calorimeter response with respect to the electron energy is another important issue. The linearity was measured to be within ±0.5%, in good agreement with Monte Carlo predictions. The lateral and vertical scans showed a constant response within ±1% over the active regions of the module.
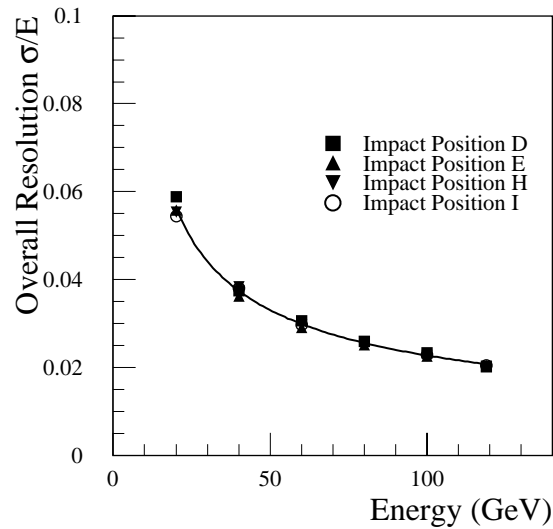
Figure 5-10 Energy dependence of the energy resolution for electrons at four different impact positions. The line shows a fit with Equation 5-5.

5.1.3.4 Results for pions

Strongly interacting particles initiate hadronic showers which cover larger regions of the calorimeter. Some of the secondary particles may exit the calorimeter, giving rise to a lateral leakage of energy. This has to be taken into consideration when comparing to simulations, before final conclusions on the energy resolution, linearity and homogeneity of the calorimeter can be made. The most active read-out cells were selected for each impact position, when reconstructing the energy. A typical cluster contained from 39 to 45 channels (see [5-14], [5-15]). Increasing the signal threshold reduced the number of read-out cells considered and therefore the noise, while giving additional signal losses which worsened the energy resolution. As for the electrons, an overall calibration constant was determined from a χ^2-minimisation of the energy resolution of all data sets. In addition, at each impact point, weight factors for the individual longitudinal compartments were determined. They mostly reflect the different sampling ratio for the modules of the rear wheel.
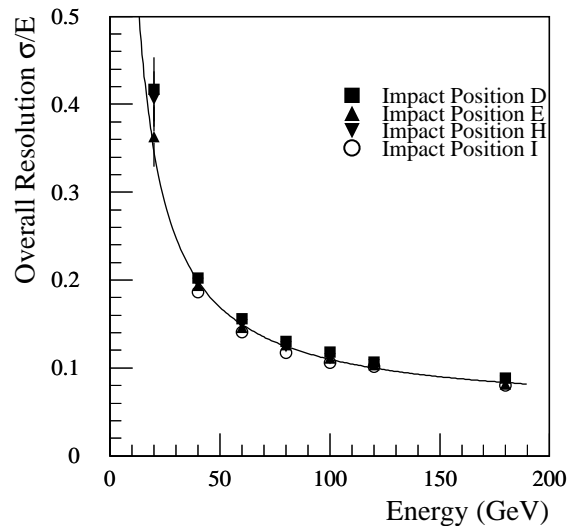
Figure 5-11 Energy dependence of the energy resolution for pions at four different impact points. These data include a contribution from electronic noise which is different for each impact beam position. The solid line, included to guide the eye, is drawn using the parameters obtained from a fit to the noise-subtracted resolution, summed in quadrature with the average electronic noise measured over the four impact positions.

For example, Figure 5-11 shows the energy resolution as a function of the pion energy for four different impact points. The electronic noise was obtained from the related cluster of read-out cells using randomly triggered events. The correlation between individual read-out cells was implicitly taken into account in the fit as well. Concerning the energy resolution, typical results are the following: for the sampling term $A = (75 \pm 2)\%\,\mathrm{GeV}^{1/2}$ and for the constant term $B = (5.0 \pm 0.3)\%$, the corresponding noise term is typically $C = 5\text{-}6\,\mathrm{GeV}$ (as fitted with Equation 5-3).

5.1.3.5 Comparison of the pion response with Monte Carlo simulation

Monte Carlo simulations modelling the test beam set-up as well as the case of full lateral coverage (see Figures 5-12 and 5-13) were performed for comparison. The signals of all read-out cells were summed in the simulation. This differs from the method employed for test beam data where the signal is reconstructed by summing read-out cells with signals above a given threshold. Effects caused by the binning in ADC units were ignored in the simulation as well. Nevertheless, the results for the energy resolution, $A = 63\%\,\mathrm{GeV}^{1/2}$ for the sampling term and $B = 5.4\%$ for the constant term, are not far from the measured values. The energy dependence of the pion response, which reflects the energy dependence of the *e/h* ratio of this non-compensating calorimeter, shows good agreement between experimental and simulated data.
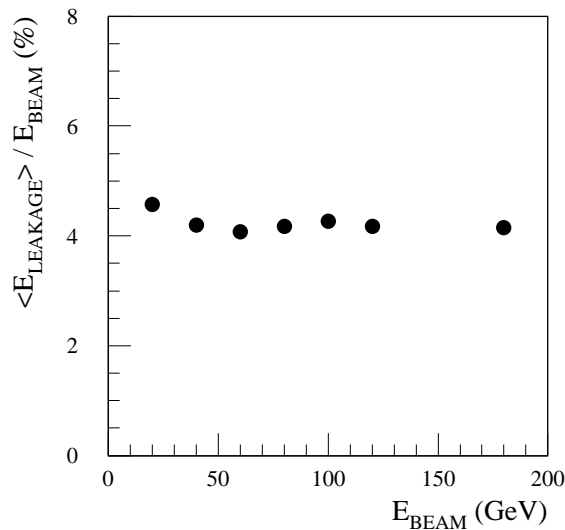

Figure 5-12 G-CALOR prediction for pions: energy dependence of the relative energy leakage as expected for the test beam set-up.
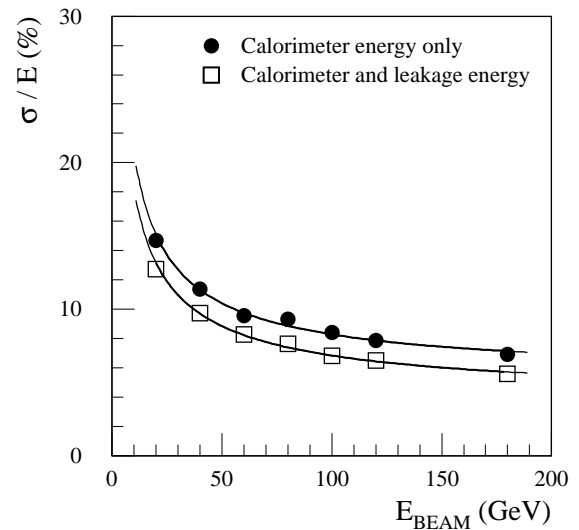
Figure 5-13 G-CALOR prediction for pions: energy resolution for the test beam set-up (solid dots) and the corresponding values for full lateral coverage (open squares). Energy dependence of the resolution is parametrised by Equation 5-5 with $A = (63 \pm 1)\%\,\mathrm{GeV}^{1/2}$, $B = (5.4 \pm 0.2)\%$ for the first set and with $A = (56.1 \pm 0.9)\%\,\mathrm{GeV}^{1/2}$, $B = (3.9 \pm 0.2)\%$ for the second one.

G-CALOR [5-6] was employed for detailed simulations. Noise was added using the response measured in randomly triggered events. To study the lateral distribution of hadronic showers, the size of the tower, used to reconstruct the pion response, was varied: a large tower, medium tower and small tower were used. The corresponding number of read-out cells was 44, 22 and 14 respectively. Figure 5-14 shows the energy resolution of the data in comparison with the predictions of G-CALOR. The noise was subtracted quadratically for both beam test and simulated data. One overall energy independent calibration constant was determined from a fit over all the energy points. In general, G-CALOR describes the data fairly well, particularly the shower core.
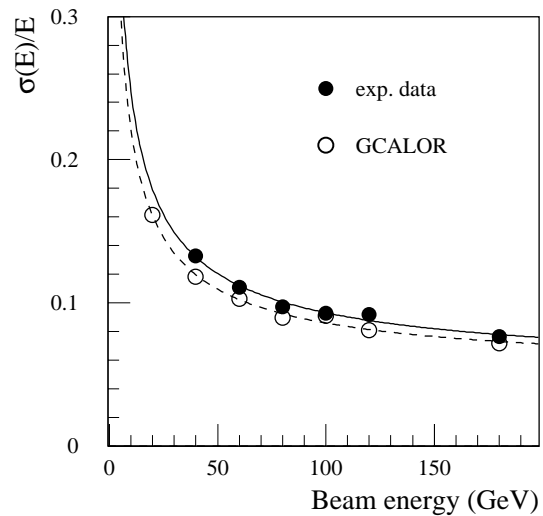

Figure 5-14 Energy resolution for pions as obtained using a large tower for the energy reconstruction. The solid dots show the data, the open circles show the predictions from G-CALOR. The lines give fits with Equation 5-5.

5.1.3.6 Results for muons

Module zero's of the HEC were also tested with a 120 GeV muon beam. Muon data are essential to provide information on the calorimeter response in the region of low energy. In addition, lateral and vertical scans allow testing the homogeneity of the calorimeter over the full depth.

Given the horizontal positioning of the calorimeter modules, the beam particles do not enter the module parallel to the read-out structure, in contrast to the actual configuration of the ATLAS detector. Therefore, twice as many read-out cells as in the final detector have to be summed to reconstruct the deposited energy of a traversing muon [5-16]. As a consequence, the noise contribution is increased and the signal to noise ratio is poorer. Nevertheless, the muon signal is well reconstructed. Figure 5-15 shows the reconstructed muon signal compared to the electronic noise obtained from identical towers of read-out cells for a few impact positions. The impact points covered both ϕ-wedges, employed with different high voltage technologies: (a) Canadian and (b) European ones. The ratio of signal to noise is about three in good agreement with Monte Carlo expectations. Figure 5-16 shows the relative muon response (response in a given cell as a fraction of the muon response in this longitudinal compartment) when scanning vertically across a few read-out cells. The read-out cell boundaries can be clearly identified and the transition to the neighbouring cell is as expected. Figure 5-17 shows the total response to 120 GeV muons. The mean value as well as the most probable (maximum) value are plotted for individual runs at different horizontal and vertical positions. The regions of increased inactive material (tie rods), where the signal is reduced, are clearly visible. The data are from the April 1998 run for both ϕ-wedges of the beam test set-up: (a) for the Canadian part and (b) for the European one. The data from the August run (c) are also shown for the Canadian ϕ-wedge. The deposited energy in the two different ϕ-wedges agrees within 1%. The ratio between the August data and the April data deviates only by 2% from unity, demonstrating the stability of the absolute calibration between the two run periods.
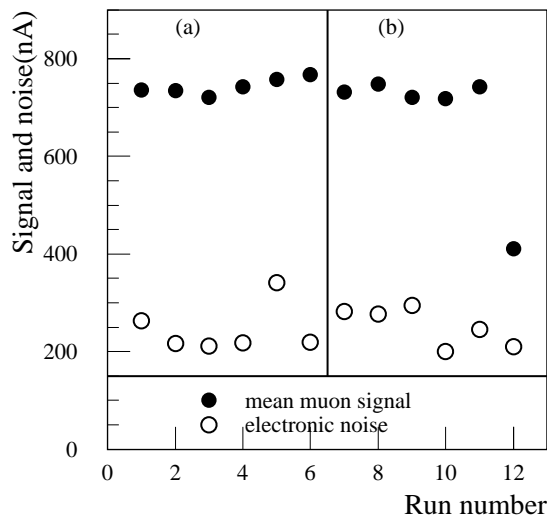
Figure 5-15 Reconstructed muon signal and electronic noise at different impact positions. The scan extends over both φ-wedges of module pairs.
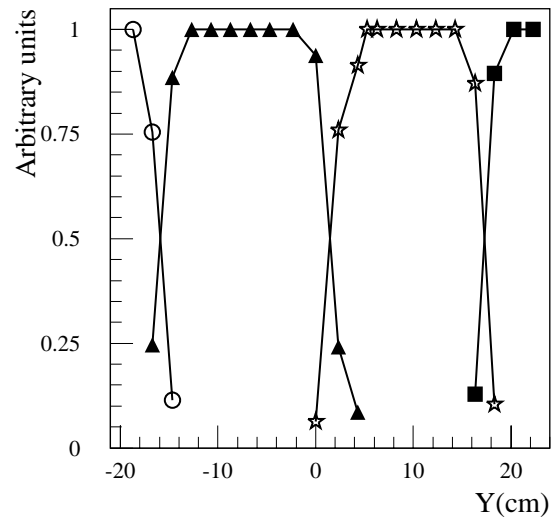
Figure 5-16 Relative muon signal in read-out cell 1 (open circles), 3 (solid triangles), 5 (stars) and 7 (solid squares) with respect to the total signal in the first longitudinal compartment as a function of impact position.

Finally, Figure 5-18 shows the distribution of the total deposited energy together with Monte Carlo expectation. The distributions agree fairly well. This holds also for the absolute value. An electron-to-muon ratio of 0.96 was obtained for data; the corresponding Monte Carlo prediction is 0.94. This corresponds to an electron to MIP (Minimum Ionising Particle) ratio of 0.83 for the data and 0.82 for the Monte Carlo.

5.1.4 Forward Calorimeter module zero test beam results

5.1.4.1 The test beam set-up

Beam tests of module zero's of the copper FCAL1 modules and the tungsten FCAL2 modules were performed in the H6 beam line at CERN. The modules were not cylindrical, but consisted of 45º sectors. These sectors are identical in construction to the final modules. The FCAL1 module contained 2350 electrodes grouped in 256 read-out channels, and the FCAL2 module contained 2550 electrodes grouped in 160 channels. Monte Carlo studies indicate that these sector modules provide 99% lateral containment for 100 GeV pions.

The modules were tested in the H1 cryostat using a beam line arrangement similar to the HEC tests. The set-up was modified mainly by adding a crude iron/scintillator 'tail catcher' calorimeter behind the cryostat. This was done in order to detect longitudinal leakage energy from the FCAL modules, as the combined length of the FCAL1 and FCAL2 modules is only 6 λ. The total length of the two modules was considerably less than the diameter of the cryostat, so liquid argon excluders made of low-density foam were positioned in front and behind the modules under test. The modules were oriented in the cryostat such that with the beam impinging on the central tile of the sector, the angle corresponded to η = 3.7 in the final detector.
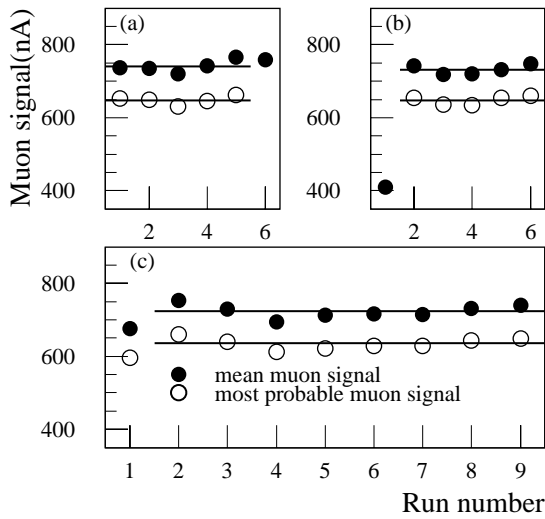
Figure 5-17 Total response to 120 GeV muons, plotted as the mean value and as the most probable (maximum) value, for individual runs at different horizontal and vertical positions. Shown are the data for (a) the Canadian and (b) the European ϕ-wedges for the April 98 run, and for the Canadian ϕ-wedge for the August 98 run (c).
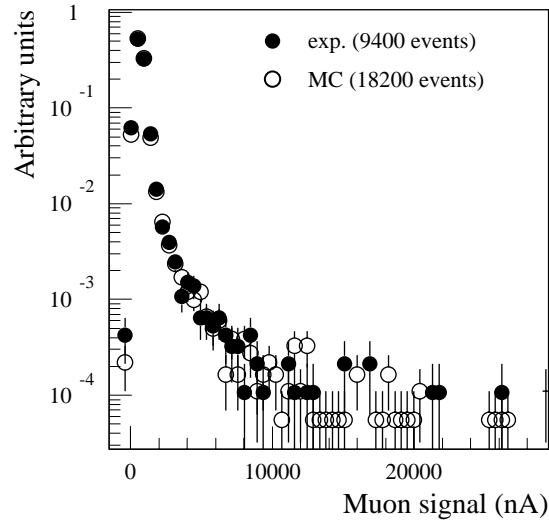
Figure 5-18 Distributions of the total response to muons of $E = 120$ GeV for the data (solid dots) and for the simulation (open circles).

The electronic read-out chain used prototypes of the signal cables, the cold transformer summing boards, and the warm feedthrough flange. So, the configuration in the cold was close to the expected final set-up. In the warm, the front-end boards and the cables between them and the feedthrough were also prototypes of the final design. This allowed meaningful measurements of the electronic noise levels to be performed.

The FCAL beam test was divided into two periods. In the first period, only the tungsten FCAL2 module was in the cryostat. This allowed measurements of the response of the FCAL2 to electrons, which gave the inter-calibration between FCAL1 and FCAL2. In the second running period, the FCAL1 module was inserted in the cryostat in front of FCAL2. This corresponded to the final configuration in the detector, and allowed measurements of the behaviour of the combined system. In both run periods data were collected with electrons and pions of energy between 20 and 200 GeV. Horizontal scans with electrons were also performed over a 16 cm range. The response at $\eta = 3.8$ was measured for muons with energy 80 and 120 GeV. These data should allow deep understanding of the FCAL performance. Here, preliminary results on the response of FCAL1 to electrons and the response of FCAL1+FCAL2 to pions are presented.

5.1.4.2 Noise performance

The major source of 'noise' in the FCAL will come from pile-up of minimum bias events, whereas the electronic noise should not play a significant role in the performance of the device. The test beam energies are small compared with the energies expected in the experiment, so the electronic noise does play a role in characterising the device from test beam data. The noise performance was determined using random-trigger events. For FCAL1 the rms noise, summed over the whole sector, corresponds to 6.8 GeV. Within a cylinder of radius 15 cm, centered on the beam direction, the noise is 4.0 GeV. The total rms noise in FCAL1+FCAL2 is 17 GeV. These are close to the expected values, and correspond to 10% of the expected pile-up at high luminosity.
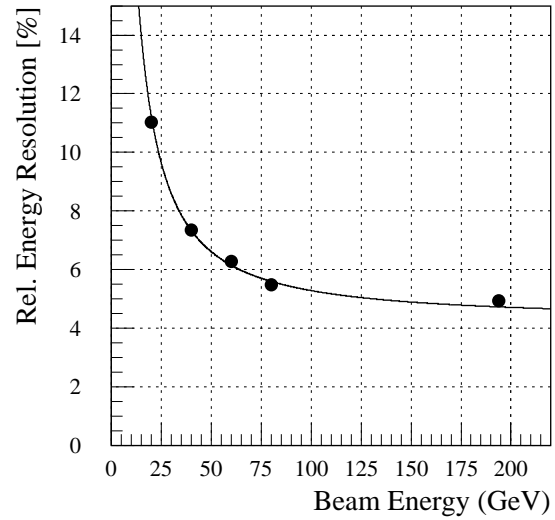

Figure 5-19 The energy dependence of the FCAL1 energy resolution for electrons. The fitted curve corresponds to the parametrisation from Equation 5-3.

5.1.4.3 Response of FCAL1 to electrons

The electron signal was studied using the energy collected over cylinders of various radii, centered on the beam impact point. This allowed the noise contribution to be minimised. In order to avoid signal saturation, the central portion of each module was instrumented with bi-gain ADC channels, and this bi-gain feature was used in the analysis. The energy resolution was parametrised using Equation 5-3. It was found that the optimum energy resolution resulted for a cylinder of radius 6 cm, the resulting fit is shown in Figure 5-19. The sampling term is better than 30% GeV$^{1/2}$ as expected, and the constant term is an acceptable 4%. The fitted values from a three-parameter fit to the resolution are given in Table 5-4. The deviation from linearity of the response was found to be smaller than 1% (see Figures 5-20 and 5-21).

5.1.4.4 Response of combined FCAL1 and FCAL2 to hadrons

In studying the response of the combined FCAL1+FCAL2 to pions, the energies in two modules were weighted with the relative response to electrons, which was determined to be

$$E = E_{FCAL1} + 2.1 \times E_{FCAL2}.$$

The small size of the hadron signals in FCAL2 resulted in electronic noise having a more sig-

Table 5-4 Terms of the electron energy resolution for FCAL1, obtained with the parametrisation from Equation 5-3.

Parameter	Fitted Value
Sampling term, A (% GeV$^{1/2}$)	26.63 ± 2.06
Constant term, B (%)	4.23 ± 0.12
Electronic noise, C (GeV)	1.70 ± 0.08

nificant contribution than in the electron runs. There are two possible approaches to allowing for the effect of electronic noise on the energy resolution. Only summing channels above some noise cut considerably reduces the level of noise per event. This results in the energy scale being non-linear, due to the effect of the noise cut varying with beam energy. Therefore results ob-
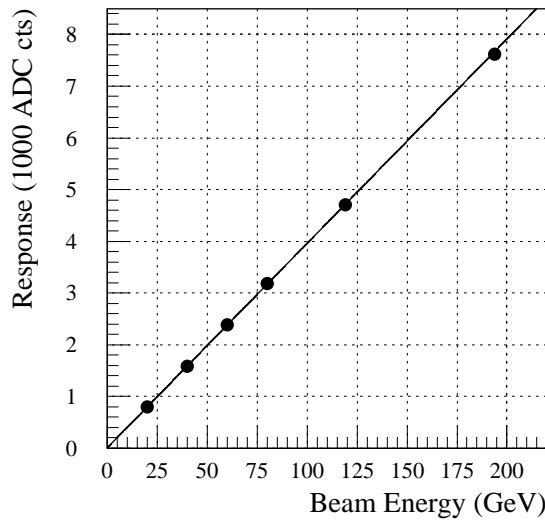
Figure 5-20 The response of the FCAL1 module as a function of the electron energy.
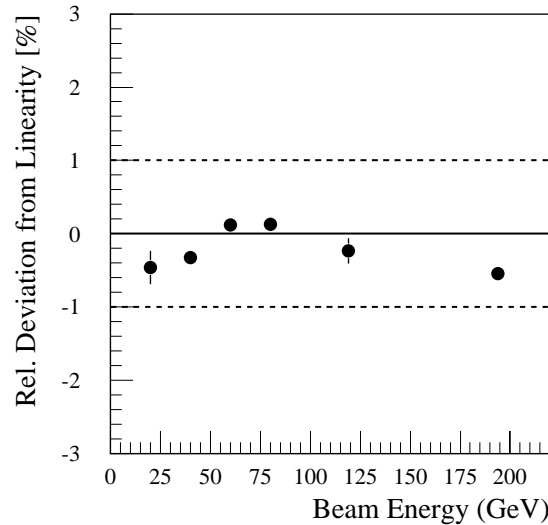

Figure 5-21 Deviation of the response of FCAL1 from linearity.

tained by summing all the energy in the modules are presented here. The noise contribution is then removed, energy by energy, by subtracting in quadrature the noise level determined from random-trigger events.

Due to the length of FCAL1+FCAL2, there is a significant amount of longitudinal energy leakage at the higher beam energies. So, from this beam test it was not possible to determine the energy resolution expected from FCAL1+FCAL2+FCAL3. Nonetheless, the tail catcher allows the study of the resolution for events with full longitudinal containment in FCAL1+FCAL2, and the resolution obtained from an unbiased sample of events with no tail catcher requirement. In fitting these results there is no need to include a noise term, and a two parameter model (see Equation 5-5), with only a sampling term A and a constant term B, is used.

The energy dependence of the energy resolution obtained for events required to have no energy in the tail catcher is shown in Figure 5-22; the fitted parameter values are given in Table 5-5. The tail catcher requirement clearly results in a biased event sample. The events will be those with a shorter shower development due, for example, to a higher than average electromagnetic portion. In general one would expect that the sampling term of $A = (81 \pm 16)\%\,\mathrm{GeV}^{1/2}$ is an optimistic estimate of the sampling term for the full

Table 5-5 Fitted values of the two parameter fit (Equation 5-5) to the FCA1+FCAL2 energy resolution for pions. The column labelled 'Tail Cut' corresponds to the fitted curve in Figure 5-22, and that labelled 'No Tail Cut' to the fitted curve in Figure 5-23.

Parameter	Tail Cut	No Tail Cut
Sampling, A (% $\mathrm{GeV}^{1/2}$)	80.9 ± 15.5	98.4 ± 10.6
Constant, B (%)	7.7 ± 1.2	10.6 ± 0.6

FCAL1+FCAL2+FCAL3 configuration. On the other hand, the constant term of $B = (8 \pm 1)\%$ may be expected to be a good measurement of the effect of inhomogeneities and channel-to-channel variations in response.

The energy resolution dependence with no requirement on the tail catcher energy deposition is shown in Figure 5-23; again the fitted parameter values are in Table 5-5. This is an unbiased sample of events, with incomplete longitudinal containment. One can expect that sampling term of $A = (98 \pm 11)\%\,\mathrm{GeV}^{1/2}$, and the constant term of $B = (10.6 \pm 0.6)\%$, are both overesti-
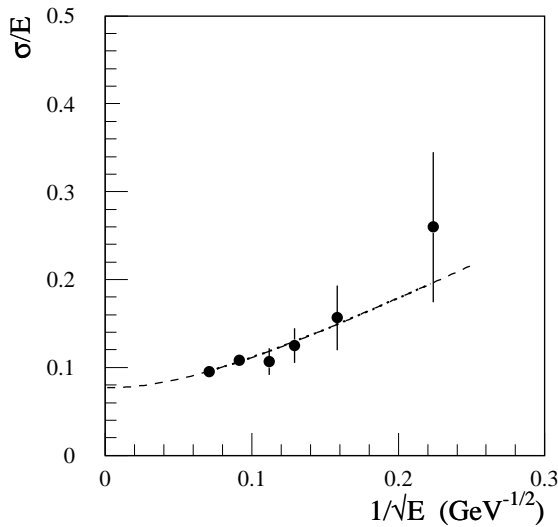
Figure 5-22 The energy dependence of the FCAL1+FCAL2 energy resolution for pions. The events were required to have no energy deposition in the tail catcher. The noise was subtracted. The solid line is a fit with a two-parameter model (Equation 5-5).
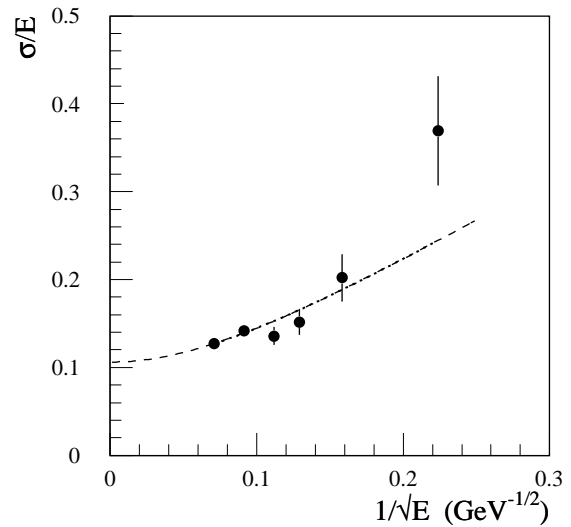
Figure 5-23 The energy dependence of the FCAL1+FCAL2 energy resolution for pions. No requirement was made on the tail catcher energy. Otherwise the treatment of the data is as in Figure 5-22.

mates of what would be expected in FCAL1+FCAL2+FCAL3. These results indicate that a final energy resolution with the sampling term $A = 100\% \, \mathrm{GeV}^{1/2}$ and the constant term $B = 7\%$, which corresponds to the ATLAS requirement, is attainable.

The results presented here are preliminary. For example no electronic calibration has been applied, and the results of studies of cross talk, noise, and deficient channels have not been taken into account.

5.2 Evolution of ATLAS calorimetry since the system TDR

Since the submission of the Calorimeter TDRs, the layout of the calorimetry has evolved towards the final design. Modifications include changes in the cryostat and dead material. The main changes to the cryostats are discussed in Section 4.1. The final read-out granularity of all calorimeters has been chosen. The update of the detector description in the simulation includes as much as possible all elements that contribute significantly to the amount of dead material, in particular rails or feet which support the detector. Here the main changes which affect simulations are summarised.

The Inner Detector rails and supports have been included. These are aluminium pieces of $\Delta\phi{\sim}5°$ and radial thickness of 13 mm located at azimuthal angles of 0° and 180° and fixed on the warm wall of the barrel cryostat. The four 8.5 cm thick iron feet supporting the barrel calorimeter are described. Each one covers partially 12° in azimuth. Barrel and end-cap rails, made mostly from aluminium, have been implemented in the simulation. All these elements introduce azimuthal asymmetry.

Stainless steel support bars of the HEC modules (thickness corresponding to 0.7 interaction lengths) are now simulated, as well as tie-rods which maintain the structural strength of the HEC copper plates. This increases the amount of dead material in front of the extended Tile Cal-

orimeter and inside the Hadronic LAr Calorimeter respectively. The modified read-out structure of the HEC has been implemented: four longitudinal compartments instead of three are now foreseen.

The shape of the cryostat wall in front of the Forward Calorimeter has changed. The outer radius of the FCAL has been reduced by 5 mm: it is now 449.5 mm (in cold) for all modules. The new read-out scheme for the FCAL has been introduced, according to which FCAL read-out channels are non-projective in azimuthal angle and pseudorapidity. The total number of electrodes is now 12 255, 10 200 and 8 532 in FCAL modules 1, 2 and 3, respectively.

5.3 Single particle performance

In this section the performance of the calorimetry for the detection of single charged hadrons and muons is reviewed. The pion energy loss in the dead material is described in Section 5.3.1 and the response to charged pions and muons in Section 5.3.2 and Section 5.3.3 respectively. Studies are based on the full simulation of the calorimeter response, done with GEANT 3.21 [5-17] and the G-CALOR hadronic shower package [5-6].

5.3.1 Energy loss in dead material across pseudorapidity

The total thickness of the ATLAS calorimetry as a function of pseudorapidity is shown in Figure 5-24. The total thickness of the active calorimeters is close to or larger than 10 λ over the full coverage up to $|\eta| = 4.9$. This figure shows also the amount of the dead material in front of the calorimeters and in the regions between the Tile and EM Calorimeters.

The energy lost in the dead material by neutral and charged pions, the two main components of a jet, is shown in Figure 5-25. The average energy lost by neutral pions (mostly in the inner wall of the cryostat and in the coil) increases from about 2% at central pseudorapidity to about 4% at $|\eta| = 1.2$. The profile of the cryostat has been designed to concentrated the dead material in a small window of about 0.2 in pseudorapidity centred at 1.45. The energy loss in this region reaches 30-35%. In the end-cap region, the loss is small, as the particles cross the cryostat walls almost perpendicularly. Significant losses appear in the crack between the end-cap and Forward Calorimeters at $|\eta| = 3.2$.

The profile of the energy lost by charged hadrons is quite different. There are two components contributing to it: the dead material in front of the calorimeter and the dead material between the electromagnetic and the hadronic calorimeters due to the outer cryostat wall. The energy loss of a charged hadron depends on the starting point of the hadronic shower. About 20% of the charged hadrons do not start showering before reaching the hadronic compartment and deposit only the energy of a minimum ionising particle. On the other hand, when the shower develops in the EM Calorimeter, the dead material is close to the shower maximum. The average energy loss is 7% with large fluctuations. In the transition region between the barrel and the end-cap, two peaks appear due to the dead material inside the vertical gap between the Tile central and extended barrel calorimeters (~12%) and due to the barrel and end-cap cryostat corners (~17%), respectively. In the end-cap region, the loss is small, except in the crack between the end-cap and Forward Calorimeters, where it is of order 8%.
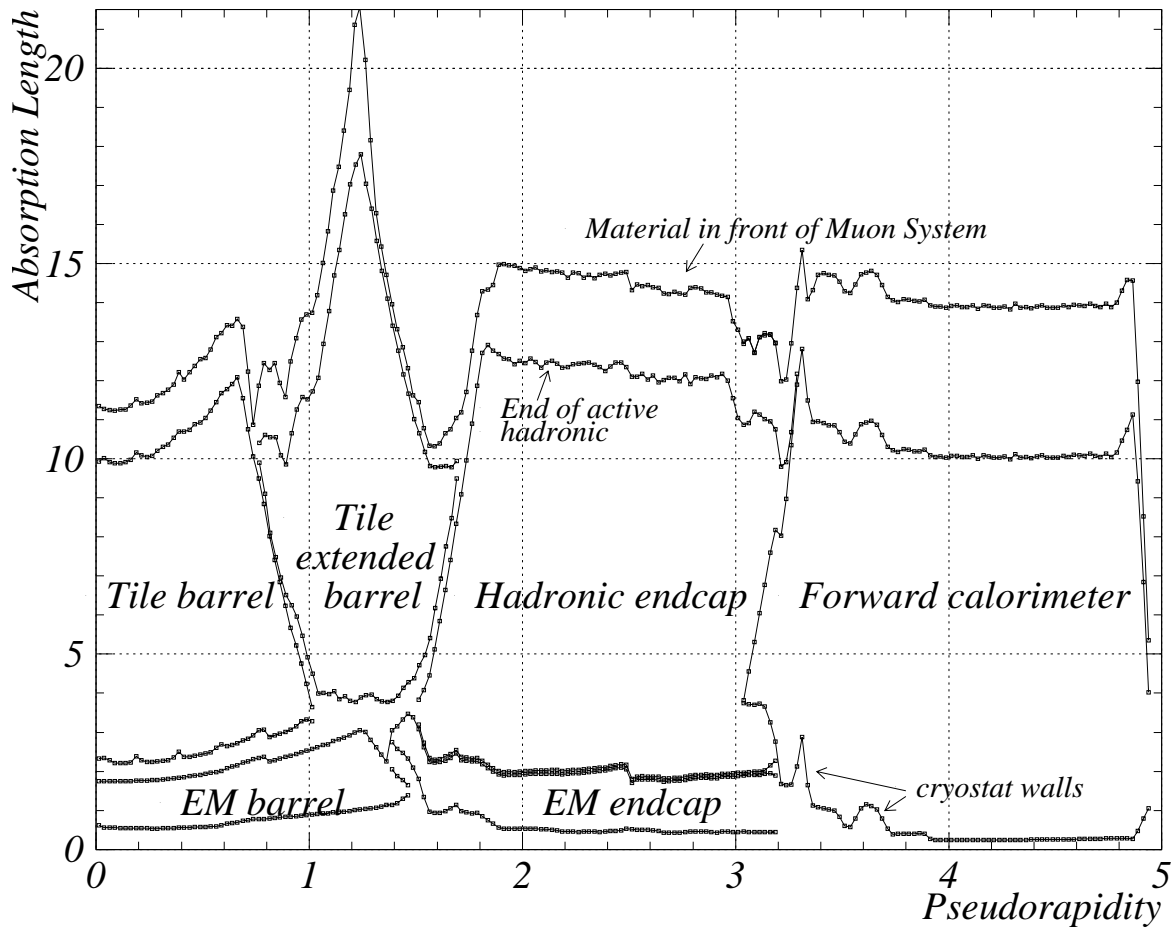
Figure 5-24 Total thickness (in absorption lengths) of the ATLAS calorimetry as a function of pseudorapidity.

5.3.2 Pion response

The performance of the hadronic calorimetry for the measurement of charged pion energy was studied. Firstly, the intrinsic energy resolution is presented in the different regions corresponding to the different calorimeter components. Then the effects of electronic noise and limited cone size are discussed.

5.3.2.1 Energy resolution

In the barrel region, the response of the calorimeter was studied at two pseudorapidity values: $\eta = 0.3$ (central barrel) and $\eta = 1.3$ (extended barrel) [5-18]. Firstly, the energy sampled in the different calorimeter compartments was converted to a total deposited energy using the electromagnetic energy scale (EM scale). Here the energy considered was not restricted to a cone and electronic noise was not added. These effects are discussed in Section 5.3.2.3. To estimate the pion energy, an algorithm similar to the Benchmark Method used to reconstruct the combined LAr-Tile test beam data (see Section 5.1.1 and Equation 5-1) was applied:

$$E_{rec} = \alpha \cdot E_{had} + \beta \cdot E_{em} + \gamma \cdot E_{em}^{2} + \delta \cdot \sqrt{E_{had1} \cdot E_{em3}} + \kappa \cdot E_{ITC} + \lambda \cdot E_{scint}. \qquad \text{5-6}$$
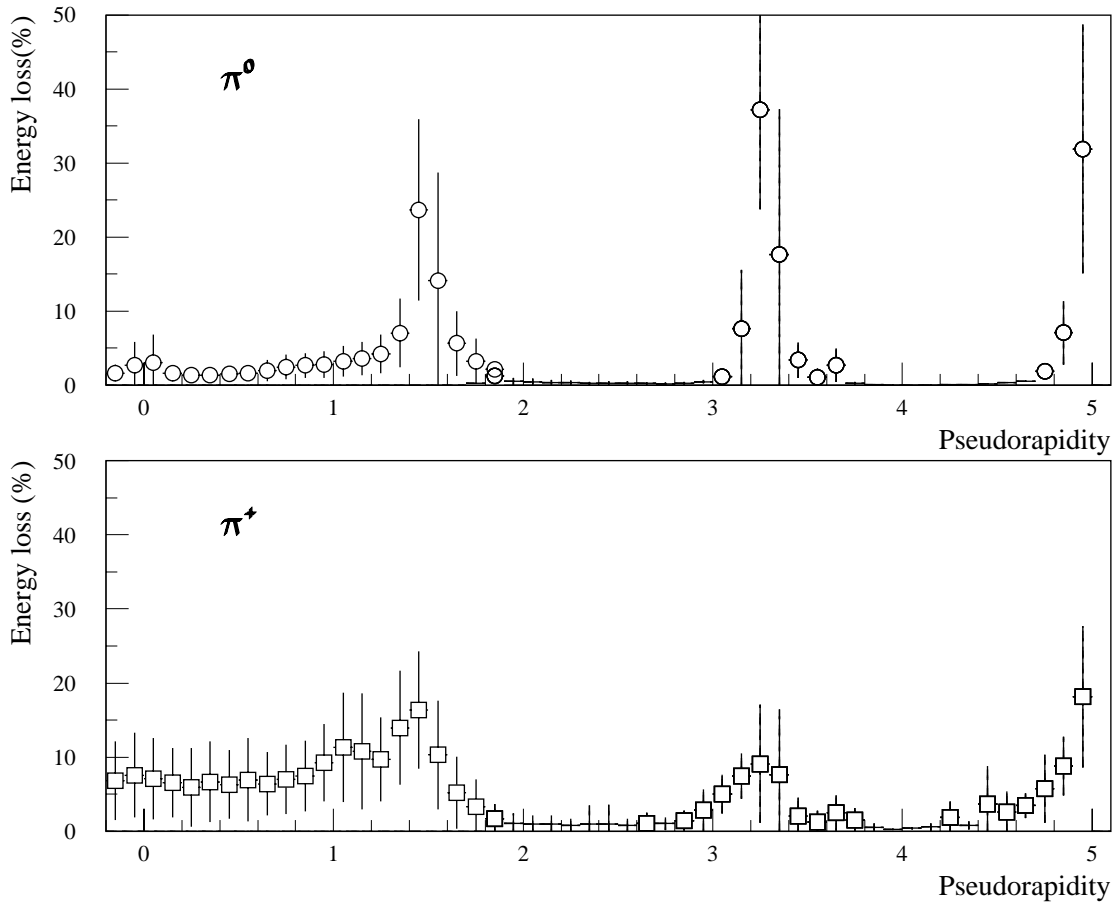
Figure 5-25 Average energy loss in the dead material as a function of pseudorapidity for neutral (top plot) and charged pions (bottom plot). The error bars correspond to the rms of the distributions.

The coefficients α and β take into account the different response of the hadronic and EM calorimeters to the pion energy. The quadratic term γE_{em}^2 provides an additional first order correction for non-compensation. The term $\delta \cdot \sqrt{E_{had1} \cdot E_{em3}}$ estimates the energy loss in the cryostat wall separating the LAr and Tile Calorimeters. In the central barrel, the energy is taken from the geometric mean of the energies in the last compartment of the LAr EM barrel and the first compartment of the Tile barrel calorimeter, whereas in the extended barrel the energy is taken from the geometric mean of the energies in the outer wheel of the EM end-cap and the first compartment of the Tile extended barrel calorimeter. The term $\kappa \cdot E_{ITC}$ corrects for the energy loss in the dead material in the vertical gap between the Tile central and extended barrels. It is sampled by the two Intermediate Tile Calorimeter (ITC) modules (see Figure 5-i). The last term $\lambda \cdot E_{scint}$ corrects for the energy loss in the barrel and end-cap vertical cryostat walls, as sampled by the three scintillators installed in that region.

The response and the energy resolution for pions in the energy range from $E_0 = 20$ GeV to 1 TeV at $\eta = 0.3$ and 1.3 are shown in Figures 5-26 and 5-27. The open crosses show the results when the coefficients of Equation 5-6 are independent of energy. There is a residual non-linearity of the pion response of the order of 4-5% between 20 GeV and 1 TeV, while the test beam data showed 10% non-linearity between 20 and 300 GeV for the Benchmark Method (see Figure 5-2), reflecting the fact that G-CALOR predicts a lower degree of non-compensation. The energy dependence of the resolution is fitted with the two-term formula (Equation 5-5). Although the res-
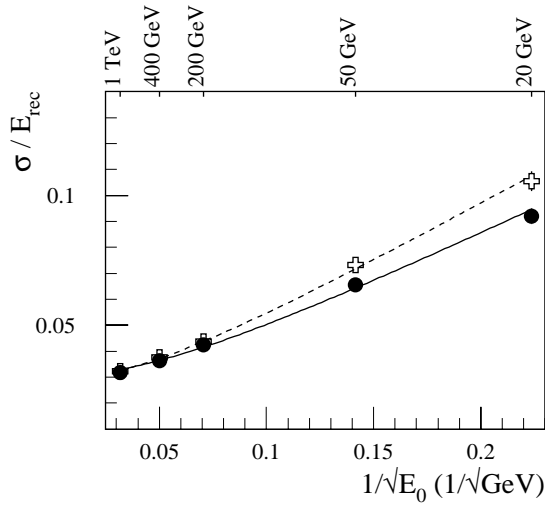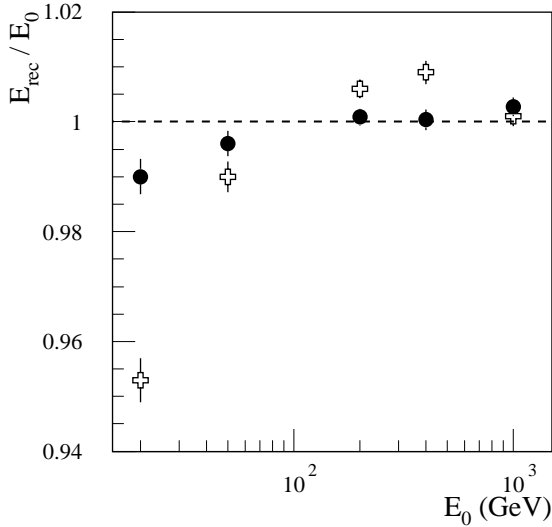
Figure 5-26 Pion energy scan in the central barrel ($\eta = 0.3$). The top plot shows the residual non-linearity, the bottom plot shows the energy resolution with the results of the fit with Equation 5-5. Two sets of parameters for the pion energy reconstruction have been used: open crosses - for energy independent parameters; solid dots - for parameters fitted at each energy and pseudorapidity.

Figure 5-27 Pion energy scan in the extended barrel ($\eta = 1.3$). The top plot shows the residual non-linearity, the bottom plot shows the energy resolution with the results of the fit with Equation 5-5. Two sets of parameters for the pion energy reconstruction have been used: open crosses - for energy independent parameters; solid dots - for parameters fitted at each energy and pseudorapidity.
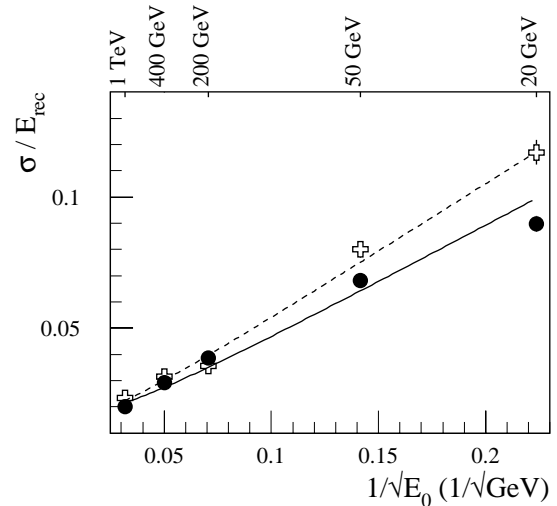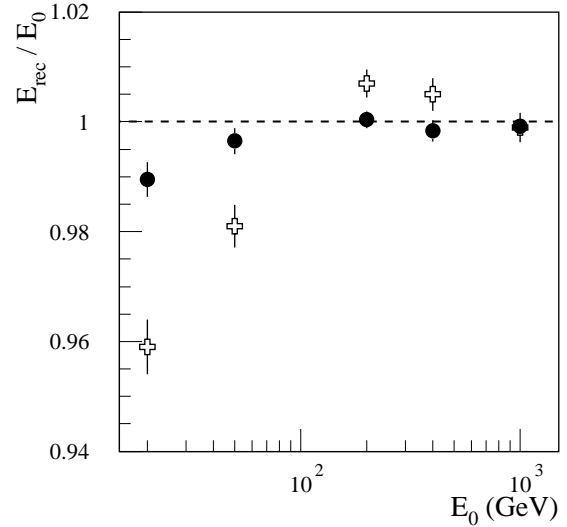
olutions obtained for low-energy pions are similar in both cases, at high energy there is some longitudinal leakage in the central barrel, yielding a resolution at 1 TeV of 3% instead of 2%, as achieved in the extended barrel. When energy dependent parameters are applied (solid dots), the linearity of the response is restored and the resolution improved. The results are the following: $A = (40 \pm 1)\%$ GeV$^{1/2}$, $B = (3.0 \pm 0.1)\%$ for $\eta = 0.3$ and $A = (44 \pm 3)\%$ GeV$^{1/2}$, $B = (1.6 \pm 0.3)\%$ for $\eta = 1.3$.

The response of the calorimeter in the end-cap region was studied with single charged pions of energies $E_0 = 100, 200, 500$ and 1000 GeV - a range of energies characteristic of the pseudorapidity coverage of the end-cap calorimeter. The pion energy is reconstructed as:

$$E_{rec} = \sum C_i \cdot E_i, \qquad\qquad 5\text{-}7$$

where E_i is the energy deposited in the different calorimeters, *i.e.* the hadronic end-cap, the EM end-cap, the Tile calorimeter with ITCs and scintillators, the EM barrel calorimeter and the Forward Calorimeter. No dead material correction term is needed here because there is no cryostat separating the EM and the hadronic parts. The parameters C_i are determined by minimising $(E_{rec}\text{-}E_0)^2$ at each energy and pseudorapidity.

In Figure 5-28 the parameters for the hadronic and EM end-cap calorimeters are shown as a function of the initial pion energy and pseudorapidity. The parameters vary significantly but smoothly with energy and pseudorapidity.
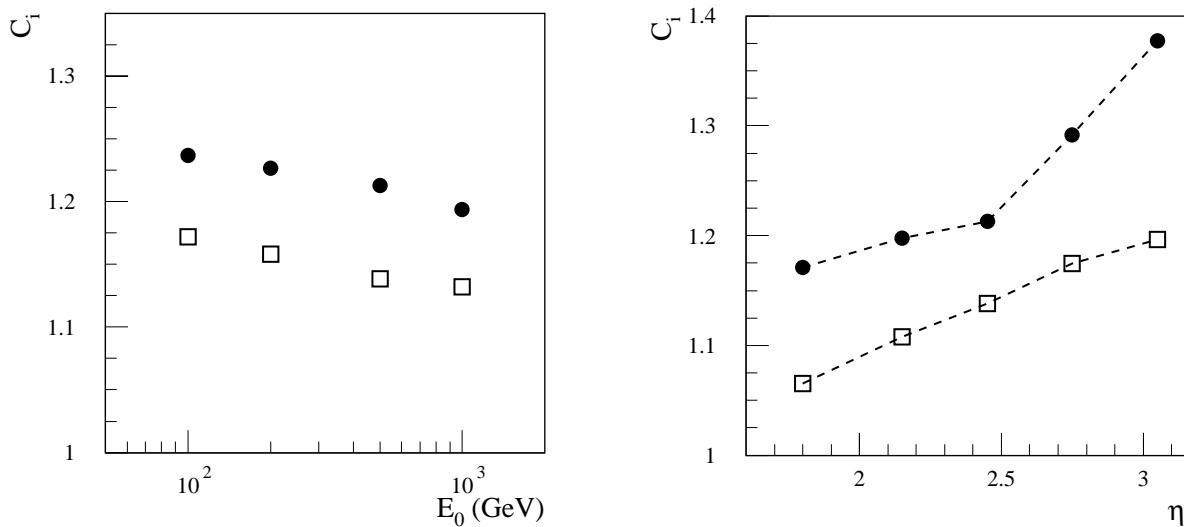
Figure 5-28 Pion energy scale parameters obtained for the hadronic end-cap calorimeter (solid dots) and for the EM end-cap calorimeter (open squares), as a function of the initial pion energy at $\eta = 2.45$ (left-hand plot) and as a function of pseudorapidity for $E_0 = 500$ GeV (right-hand plot).

In Figure 5-29 the sampling and constant terms of the pion energy resolution, obtained by the fit with the two-term formula (Equation 5-5), are plotted (solid dots) as a function of the pion pseudorapidity. In the pseudorapidity range $1.8 < |\eta| < 3.05$, covered by the end-cap calorimeters, these terms are fairly stable: $A = 55\text{-}60\%$ GeV$^{1/2}$, $B = 2.5\text{-}3.0\%$. The effect of restricting the reconstruction to a cone around the pion direction is discussed in Section 5.3.2.3.

5.3.2.2 Pseudorapidity scan

A pseudorapidity scan with pions of constant transverse energy $E_T = 20$ and 50 GeV was carried out to check that the linearity of the response can be maintained and that no significant tail appears in the line shape. In the central and extended barrel region, the algorithm, characterised by Equation 5-6, with energy and pseudorapidity dependent parameters was applied. The resulting distribution of the mean fitted responses was a Gaussian with $\sigma = 2.6\%$ for pions of $E_T = 20$ GeV and $\sigma = 1.5\%$ for pions of $E_T = 50$ GeV. In the end-cap and forward regions, the procedure to reconstruct pion energies was similar to the one described by Equation 5-7. The only difference was that the energy depositions in individual longitudinal compartments of the hadronic and EM end-cap calorimeters and of the Forward Calorimeter were used for the terms E_i.
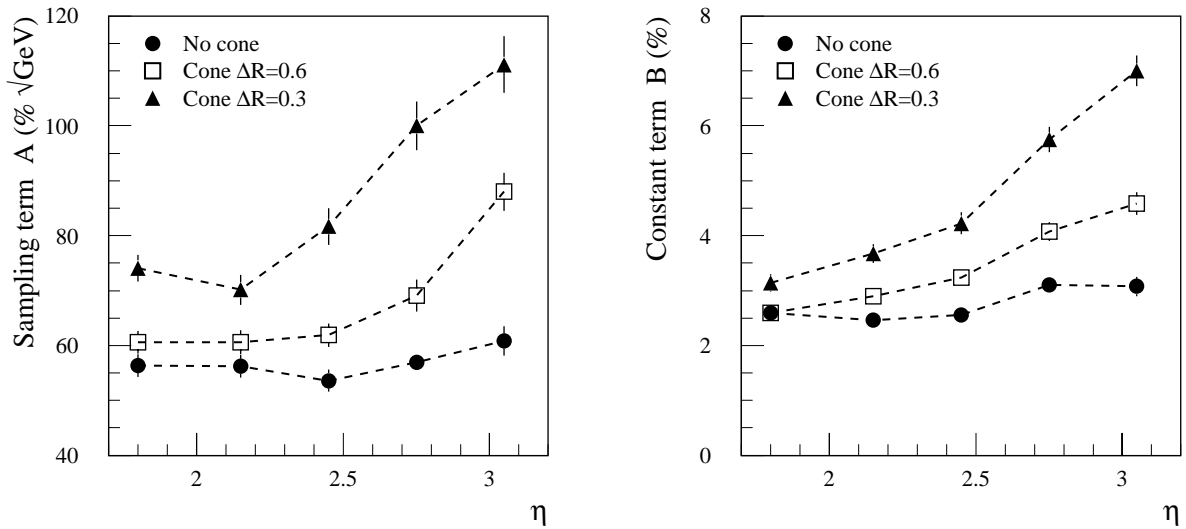
Figure 5-29 Pseudorapidity dependence of the sampling and constant terms of the energy resolution for single charged pions in the end-cap region. The solid dots show the results obtained without restriction on the reconstruction volume; open squares - with a pion reconstruction cone of $\Delta R = 0.6$; triangles - with a pion reconstruction cone of $\Delta R = 0.3$.

The energy resolutions obtained for the two scans are shown in Figure 5-30. The solid lines show the goal for the jet energy resolution of the ATLAS hadronic calorimetry in the region $|\eta| < 3$, set out in [5-1]. The pion energy resolution is close to this line and even better at some pseudorapidities. In the regions of the cracks between the calorimeters (around $|\eta| = 1.5$ and $|\eta| = 3.2$), where the amount of dead material is the largest, the resolution is somewhat worse. At a pseudorapidity of 4.8, close to the edge of the FCAL, the lateral leakage from the calorimeters starts to be important and leads to a significant degradation of the resolution.
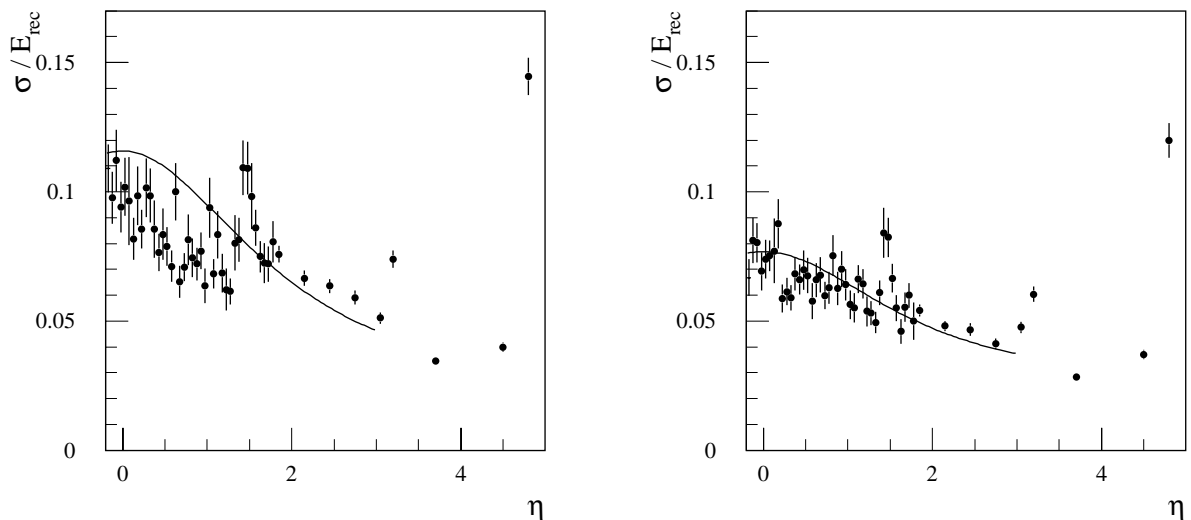

Figure 5-30 The dependence of the energy resolution on pseudorapidity for charged pions of constant transverse energy: $E_T = 20$ GeV (left-hand plot) and $E_T = 50$ GeV (right-hand plot). The lines correspond to the energy resolution parametrised using Equation 5-5 with $A = 50\%$ GeV$^{1/2}$ and $B = 3\%$.

In addition, the tails of the distributions of the reconstructed energy were investigated. Figure 5-31 shows the events with a pion response more than three standard deviations away from the mean. No significant tails are present: the fraction of events in the tails does not exceed 1-2%. A few events out of a total of 5000 events per energy scan, mostly from the sample of pions of $E_T = 20$ GeV, deposit relatively little energy. These correspond to pions decaying to muons before reaching the calorimeter.
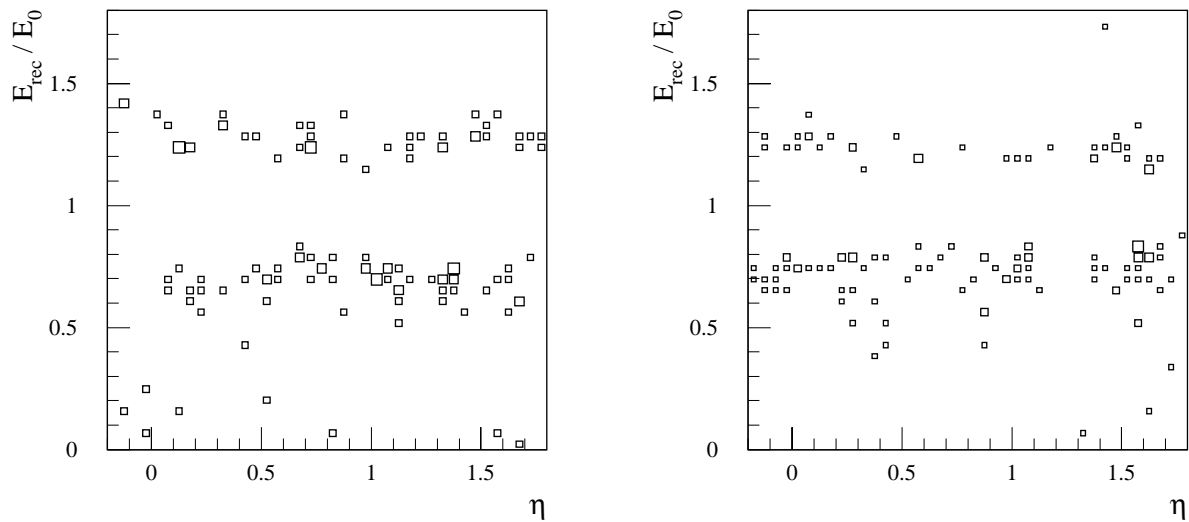

Figure 5-31 Events in the tails of the distribution of the reconstructed energy as a function of pseudorapidity for pions of $E_T = 20$ GeV (left-hand plot) and for pions of $E_T = 50$ GeV (right-hand plot). Tails are defined as events with reconstructed energies more than three standard deviations away from the mean.

5.3.2.3 Effects of electronic noise and cone size

The results presented so far were obtained without any restriction on the pion reconstruction volume. These results characterise the intrinsic performance of the calorimeters. The presence of electronic noise does not allow integration over too wide a region, therefore the measurement of the pion energy must be restricted to a cone $\Delta R = \sqrt{\Delta^2 \eta + \Delta^2 \phi}$. A compromise has to be found between the pion energy lost outside of this cone and the noise included inside. The optimum varies as a function of pseudorapidity, since the showers have a width which is characterised by the polar angle whereas the calorimeter cells subtend intervals of constant pseudorapidity. Hence, at higher values of pseudorapidity, the showers extend laterally over more cells.

In Figure 5-32 the electronic noise in a cone is shown as a function of pseudorapidity. For a cone of $\Delta R = 0.6$, noise is above 3 GeV even in the barrel region. Digital filtering [5-13] allows noise suppression (approximately by a factor 1.6). But even this level of noise is large and is comparable to the intrinsic resolution of the calorimeters for pions with energy of a few tens of GeV. A smaller cone of $\Delta R = 0.3$ is preferable from this point of view; after digital filtering, noise can be kept around 1 GeV in the barrel region and below 3 GeV in the transition region between the barrel and the end-cap. The levels of electronic noise in the different calorimeters in towers of $\Delta\eta \times \Delta\phi = 0.1 \times 0.1$ are presented in Table 5-6.
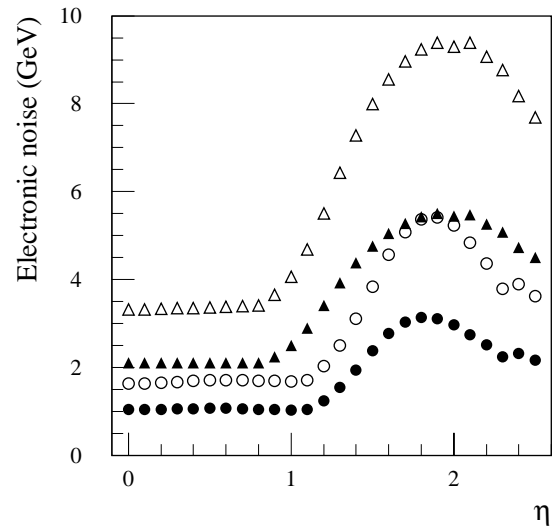

Figure 5-32 Level of electronic noise in the calorimeter (in EM scale) as a function of pseudorapidity. The triangles (dots) show the noise for a cone of $\Delta R = 0.6$ ($\Delta R = 0.3$). Open symbols correspond to the normal electronic noise, solid symbols correspond to the noise after digital filtering.

The response and the energy resolution in the barrel region are presented in Figures 5-33 and 5-34 as a function of the cone size used for the pion energy reconstruction. Energy losses outside a cone noticeably increase with decreasing cone size, especially for 50 GeV pions. The energy resolution also becomes worse, but it is still acceptable for the cone of $\Delta R = 0.3$.

Table 5-6 Electronic noise (in EM scale) in the calorimeter tower of $\Delta\eta \times \Delta\phi = 0.1 \times 0.1$, obtained after digital filtering.

Central barrel region $\eta = 0.3$		Extended barrel region $\eta = 1.3$		End-cap region $\eta = 2.45$	
Calorimeter	Noise (GeV)	Calorimeter	Noise (GeV)	Calorimeter	Noise (GeV)
Tile	0.056	Tile	0.047	Hadronic end-cap	0.366
EM barrel	0.164	EM barrel	0.151	EM end-cap	0.113
Presampler	0.098	Presampler	0.107		
Total	0.199	Total	0.191	Total	0.384

In the end-cap region, the worsening of the energy resolution with decreasing cone size is more pronounced, especially in the region $|\eta| > 2.5$. This can be seen in Figure 5-29.

Selecting cells with energy deposition above a certain threshold decreases the noise contribution. Studies made for pions in the barrel region enabled optimisation of the cone size and of the noise cut to obtain the best energy resolution. In Figure 5-35, the energy dependency of the resolution is plotted for two pseudorapidities: $\eta = 0.3$ and $\eta = 1.3$. Results of the fit of these dependencies with the standard formulae are presented in Table 5-7. Using a 2σ-noise cut to select calorimeter cells within the cone of $\Delta R = 0.3$ leads finally to the best energy resolution, when electronic noise is taken into account. However, in comparison to the ideal case, *i.e.* without noise and without a cut on the cone size (see Section 5.3.2.1 or the first row in Table 5-7), the sampling and the constant term (especially in the extended barrel region) become worse.
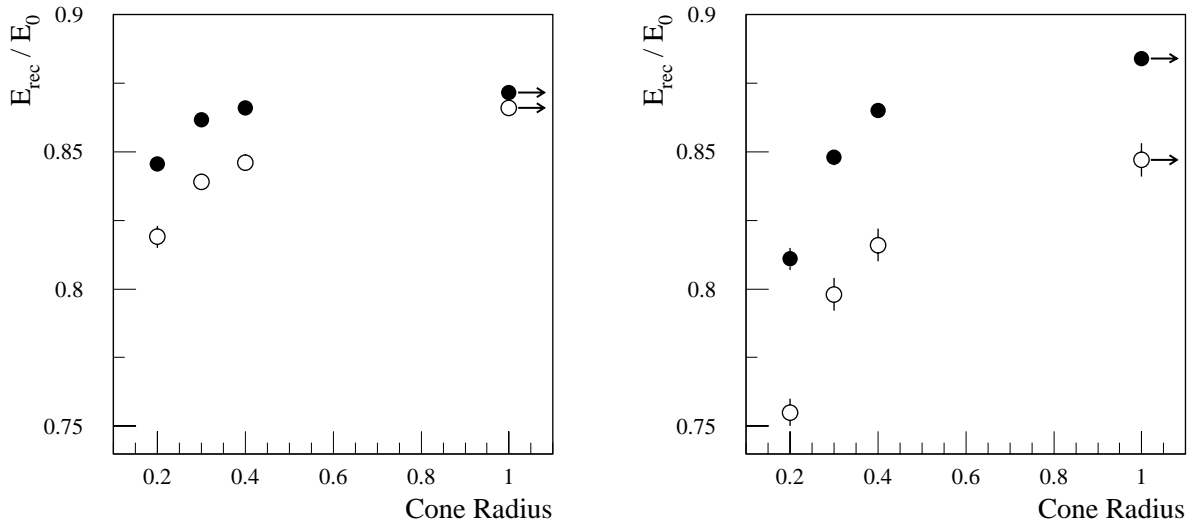
Figure 5-33 Energy response for 50 GeV (open circles) and 200 GeV (solid dots) charged pions at $\eta = 0.3$ (left-hand plot) and at $\eta = 1.3$ (right-hand plot) as a function of the cone size. The points with arrows correspond to the case without a cone restriction. Energy and pseudorapidity independent parameters were used for the energy reconstruction (see Equation 5-6).
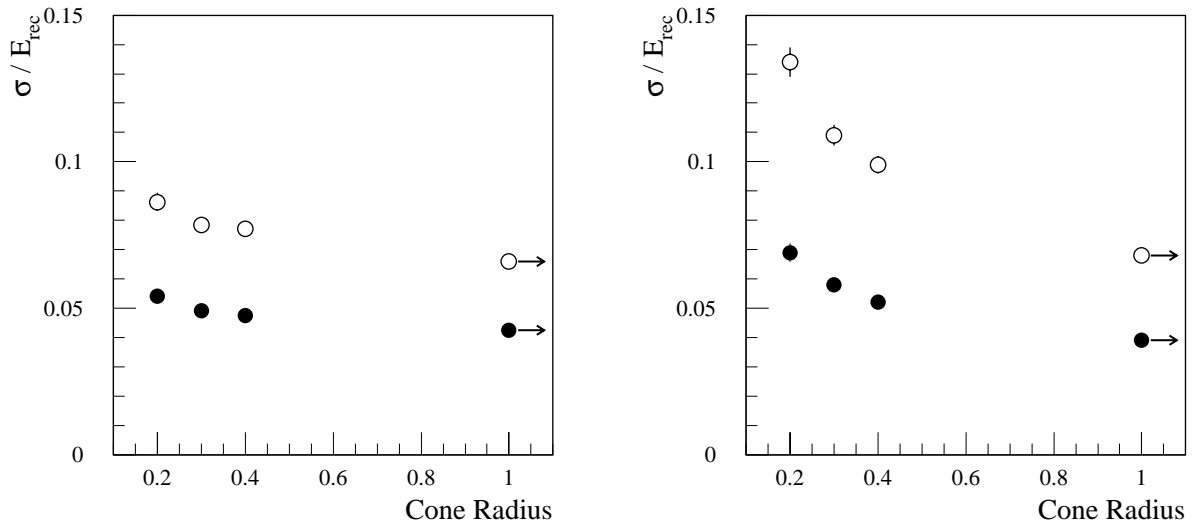
Figure 5-34 Energy resolution for 50 GeV (open circles) and 200 GeV (solid dots) charged pions at $\eta = 0.3$ (left-hand plot) and at $\eta = 1.3$ (right-hand plot) as a function of the cone size. The points with arrows correspond to the case without a cut on the cone size. Energy and pseudorapidity dependent parameters were used for the energy reconstruction (see Equation 5-6).

5.3.3 Muon response

The response of the hadronic compartments to isolated muons was studied. Figure 5-36 (left-hand plot) shows the energy deposited by 100 GeV muons in the Tile Calorimeter as a function of pseudorapidity. The open circles show test beam results. The barrel and extended barrel module zero's have been exposed to muons of 100 GeV at various pseudorapidity values. The most probable value (MOP) resulting from a fit with a Landau distribution convoluted with a Gaussian to the experimental muon spectrum is shown (see Section 5.1.2.3 and Figure 5-9). Typ-

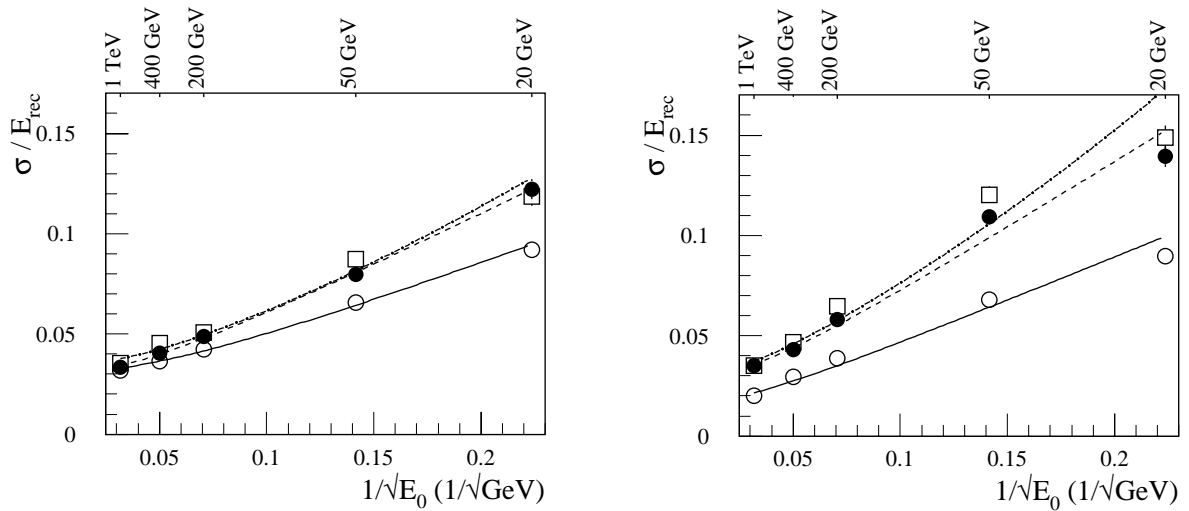**Figure 5-35** Energy dependence of the resolution for pions at $\eta = 0.3$ (left-hand plot) and at $\eta = 1.3$ (right-hand plot). The open circles show results obtained without a cut on the cone size and without electronic noise. The solid dots show results obtained for a cone of $\Delta R = 0.3$ and without electronic noise. The open squares show results obtained for a cone of $\Delta R = 0.3$ with a 2σ-noise cut (when electronic noise was included). Curves show the results of fits with the two-term formula (Equation 5-5) for the first two sets and with the three-term formula (Equation 5-3) for the third set.

Table 5-7 Terms of the pion energy resolution fitted with the two-term (Equation 5-5) and the three-term (Equation 5-3) expressions.

	Central barrel region $\eta = 0.3$			**Extended barrel region** $\eta = 1.3$		
	A (% GeV$^{1/2}$)	*B* (%)	*C* (GeV)	*A* (% GeV$^{1/2}$)	*B* (%)	*C* (GeV)
No cone, no noise	40 ± 1	3.0 ± 0.1	-	44 ± 3	1.6 ± 0.3	-
Cone $\Delta R = 0.3$, no noise	53 ± 2	3.0 ± 0.2	-	67 ± 4	2.9 ± 0.4	-
Cone $\Delta R = 0.3$, noise with a 2σ-cut	50 ± 4	3.4 ± 0.3	fixed at 1.0	68 ± 8	3.0 ± 0.7	fixed at 1.5

ical values in the barrel are 2 GeV for the MOP and 400 MeV for the σ on the left-hand side of the peak. The level of expected electronic noise when summing typically six cells (12 PMTs) is about 70 MeV, hence, the signal is well separated from the noise. In the region of the vertical crack between the barrel and extended barrel section, the thickness of active calorimeter is reduced. Figure 5-36 shows also the Monte Carlo prediction for the muon signal when the energy deposited in the ITCs is added. Full efficiency is then reached.

Inside jets, muons may overlap with other particles. Low-p_T pions tend to be absorbed in the inner part of the calorimeter while muons are much more penetrating. At high luminosity, minimum bias events will deposit more energy in the innermost compartments. The rms of the energy deposition by minimum bias events is about 100-150 MeV in the first two compartments and decreases to only 10-15 MeV in the last compartment [5-3]. Hence an efficient muon detection in the outermost compartment provides a useful muon tagging tool. Figure 5-36 (right-hand plot) shows the response in the last compartment. Experimental data from the barrel and extended barrel are compared to the Monte Carlo prediction when the energy in the ITCs has
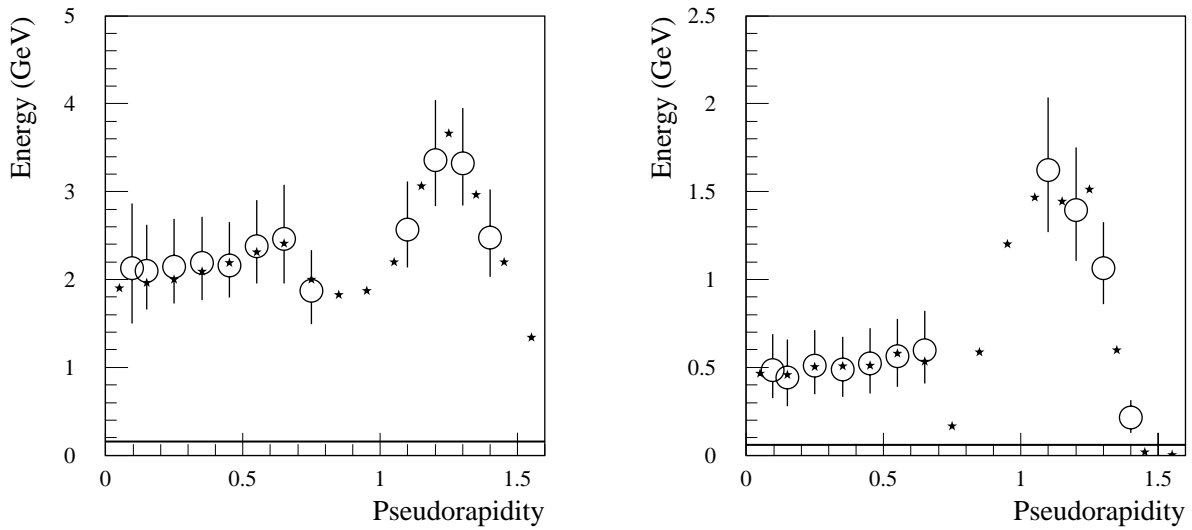
Figure 5-36 Total deposited energy (left-hand plot) and energy deposited in the outermost compartment (right-hand plot) by 100 GeV muons in the pseudorapidity range covered by the Tile Calorimeter. The open circles show results from the test beam. The error bars show the asymmetric contribution to the FWHM. The stars represent the simulated response in the ATLAS set-up, including the signal in the ITCs. The solid lines show the expected level of electronic noise.

been added. Only the pseudorapidity gap between 0.7 and 0.8 is not efficiently covered. For very central pseudorapidity ($|\eta| < 0.075$), the muon trajectories are almost parallel to the staggered iron-scintillator structure and the signal varies strongly as a function of the impact point. The efficiency to detect a muon in the last compartment only with a 3σ significance above the electronic noise is reduced to 80% in that pseudorapidity interval. If the total signal in the calorimeter is used, then full efficiency is restored.

The effect of pile-up on the muon signal has been studied. Figure 5-37 (top left) shows the signal deposited by muons of $E_T = 20$ GeV in the Tile barrel calorimeter ($0.2 < |\eta| < 0.6$) without (solid line) and with (dashed line) minimum bias events included. The effect is small: the minimum bias events deposit in average 150 MeV along the muon track with an rms of 210 MeV. This has to be compared to the average 2.4 GeV deposited by the muon in the calorimeter. Figure 5-37 (top right) shows the signal deposited by muons in the last compartment of the calorimeter. The level of energy deposited by minimum bias events in that case is on average 32 MeV with an rms of 45 MeV, to be compared to the average energy deposited by muons of 0.6 GeV.

The bottom plots in Figure 5-37 show the fraction of events which passed an energy threshold cut for minimum bias events (solid line) and for muons (dashed line). An efficiency of 99% for muons is obtained with a fake rate of the order of 0.5%, both for the full calorimeter and for the third compartment. These are the basic performance numbers, which will be masked by other effects, such as the acceptance, the road in the calorimeter used for muon reconstruction, the overlap with other particles in the event. These effects have to be evaluated in their context: on-line trigger or off-line analysis.

A preliminary study of muon detection in the hadronic end-cap calorimeter was done. The total noise consists of two parts: electronic noise and noise due to pile-up of minimum bias events. The use of multi-sampling read-out and the digital filtering method allows suppression of the total noise. The degree of suppression depends on the relative contributions of electronic and
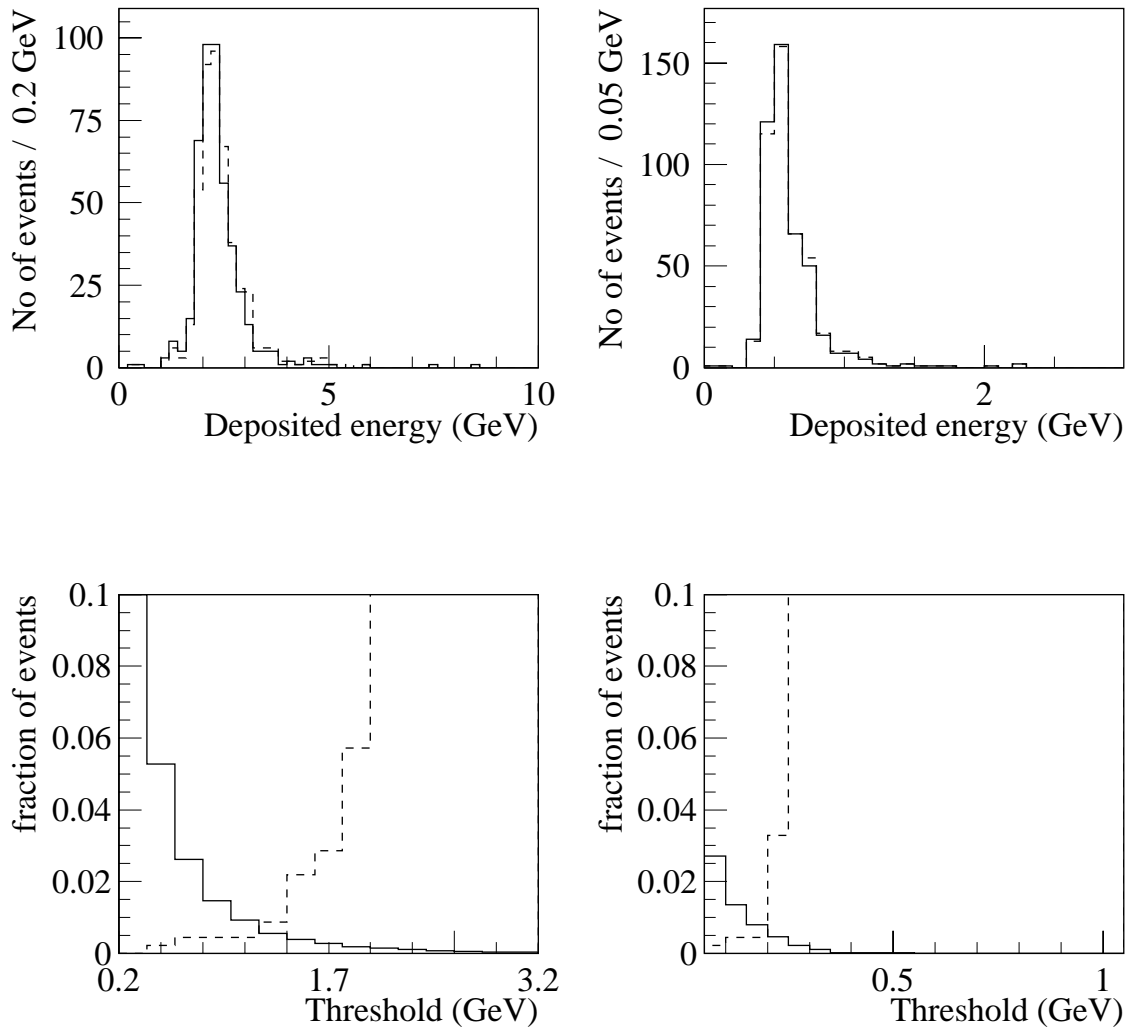
Figure 5-37 Top: energy depositions in the Tile barrel calorimeter by muons of $E_T = 20$ GeV without (solid line) and with (dashed line) minimum bias events included. Bottom: the fraction of minimum bias events that are kept (solid line) and the fraction of signal events with muons that are lost (dashed line) as a function of the threshold applied. The left-hand plots correspond to the full calorimeter, the right-hand plots correspond to the third compartment only.

pile-up noise and on the parameters of the electronics chain. As an example, in Figure 5-38 the ratio of the signal from a minimum ionising particle (MIP) and the noise in a cell of the hadronic end-cap calorimeter is presented. For optimised values of the parameters of the electronics, even at the highest luminosity, it is possible to keep this ratio above 2.5 in the last longitudinal compartment for $|\eta| < 2.5$.
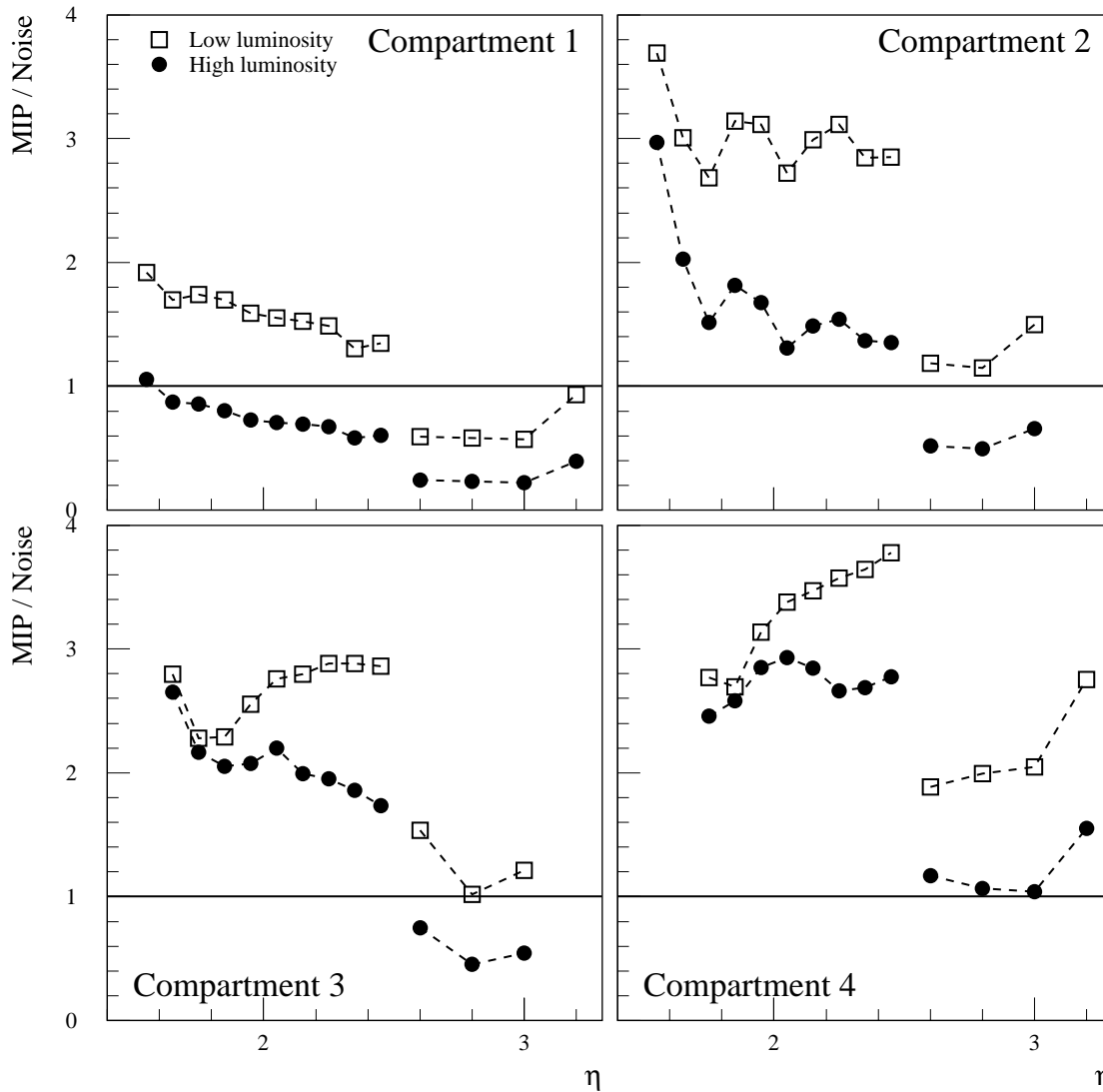
Figure 5-38 Expected ratio of the signal from a minimum ionising particle (MIP) and the noise in a cell of the hadronic end-cap calorimeter. The noise is calculated after digital filtering, applied for two values of luminosity.

5.4 Calibration with *E/p* from single hadrons

5.4.1 Introduction

The detection of single charged isolated hadrons from $\tau \rightarrow h\nu$ decays [5-19] where the charged hadron can either be a pion or a kaon can be used to transfer the calibration from the test beam to the actual detector and to inter-calibrate the various regions of the calorimeter. The precise measurement of their momentum *p* in the tracking detectors, compared to the energy *E* measured in the calorimeters could, in addition, provide a cross-calibration between these detectors.

All processes generating isolated single charged hadrons are potentially useful. For simplicity, the signal considered here [5-20], containing an isolated charged pion coming from τ decay ($\tau \rightarrow \pi\nu$ with a branching ratio of 11.08%), is Drell-Yan *W* production followed by the decay

$W \to \tau\nu$. The event rate is large and this process could therefore provide a calibration sample over a large energy range. The lower energy range is constrained by the trigger requirements whereas the upper is limited by production kinematics: 60 GeV in the barrel calorimeter, 120 GeV in the extended barrel and 250 GeV in the end-cap calorimeters. The main difficulty with this calibration method arises from background events where the π is accompanied by one or more photons from π^0 decay which could distort the energy measurement. These events must be rejected by isolation and shower shape cuts that do not bias the measurement for the *E/p* matching to be effective. This background is considered below.

Despite the fact that QCD backgrounds are potentially huge, clean signals from $W \to l\nu$ have been observed at hadron colliders [5-21]. The combination of E_T^{miss} and τ identification using isolation should be sufficient to reduce the QCD background to a level below 10% of the signal. Nevertheless, studies need to be done to demonstrate that the residual QCD background does not distort the *E/p* calibration with isolated charged pions beyond 1% which is the goal of this method.

5.4.2 Signal and backgrounds

W events were generated with PYTHIA 6.122 [5-22] (without pile-up of minimum bias events). The τ decay was performed with TAUOLA 2.6 [5-23]. The fast simulation package ATLFAST 2.20 [5-24] was used to simulate the ATLAS detector response. Table 5-8 summarises the τ decay channels that are studied and their branching ratios.

The distributions of the transverse momentum of charged pions and of E_T^{miss} are shown in Figure 5-39. The charged pions are distributed uniformly in pseudorapidity in the range covered by the Inner Detector.
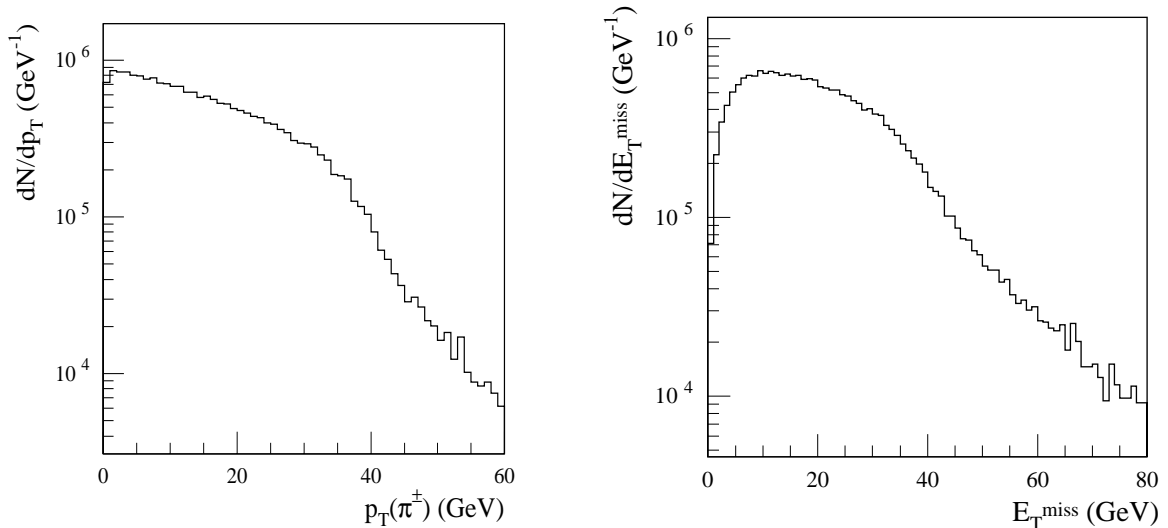

Figure 5-39 Distributions of the transverse momentum of charged pions from $\tau \to \pi\nu$ decays (left-hand plot) and missing transverse energy (right-hand plot) for the $W \to \tau\nu$ events, for an integrated luminosity of 10 fb-1.

Since QCD backgrounds are assumed to be small the most dangerous source of background are the τ decays to more than one prong or containing neutral pions which remain undetected in the tracking detectors. The relevant decay modes are those with one charged particle and with at least one neutral pion ($\tau \rightarrow h\nu + n\pi^0$ ($n \geq 1$) with the branching ratio of 37.0%) and those with multi-prongs ($\tau \rightarrow hhh\nu + n\pi^0$ ($n \geq 0$) with a branching ratio of 14.9%). The most dangerous backgrounds are those coming from τ decay to one charged hadron accompanied by neutral pions, because the additional energy deposited by the π^0 in the calorimeters biases the *E/p* ratio. Moreover, the exclusive decay channel that has the largest branching ratio has also a topology which is very similar to the one of the signals, namely $\tau \rightarrow \rho\nu$ with $\rho \rightarrow \pi\pi^0$ and branching ratio is 24.2%.

5.4.3 Event selection and results

5.4.3.1 Trigger

The specific trigger available at low luminosity for the signal channel is the τ-jet trigger combined with the missing E_T trigger. At LVL1, the trigger is T20+XE30; the jet has $p_T > 20$ GeV and there is at least 30 GeV of E_T^{miss}, for details see Section 11.2.5.2. The LVL2 trigger is discussed in Section 11.4.4. At level 2 the τ identification cuts are tightened; the rate for the τ20+xE30 LVL2 trigger is estimated to be 400 Hz at low luminosity (Section 11.7.3.3). A simulation of the LVL1 trigger was performed in order to estimate the efficiency for each of the τ decay modes. It gives a total rate from $W \rightarrow \tau\nu$ of 0.16 Hz. Table 5-8 summarises the trigger efficiency for τ decay modes studied in $W \rightarrow \tau\nu$ production. The number of expected signal events, for 10 fb^{-1} is 1.59×10^6 while the number of background events from τ decays with neutral pions is 9.43×10^6.

Table 5-8 Branching ratios, trigger, preselection and selection efficiencies for $W \rightarrow \tau\nu$ events. The number of expected events that pass the selection criteria are given for integrated luminosity of 10 fb^{-1}.

τ decay mode	τ branching ratio	Trigger efficiency (%)	Preselection efficiency (%)	Selection efficiency (%)	Number of events
single pion	11.1	7.4	2.3	1.80	3.9×10^5
$\rho \rightarrow 2\pi$ mode	24.2	11.4	2.2	0.27	1.2×10^5
$a_1 \rightarrow 3\pi$ mode	13.00	15.4	0.9	0.04	9.3×10^4
K^* mode	1.3	10.2	1.8	0.36	8.5×10^3
$3\pi^{\pm}\pi^0$ mode	1.5	17.3	0.1	0.02	1.5×10^2

5.4.3.2 Event Selection

The signal consists of a single isolated charged energetic hadron which is detected in the Inner Detector as a single isolated track and in the calorimeter as a narrow jet. A cone of $\Delta R = 0.15$, centered on the jet direction was constructed and events with one and only one charged track

inside the cone were accepted. Table 5-8 summarises the preselection efficiencies of τ decay modes in the $W \to \tau\nu$ events. Since the topology of the signal and the $\tau \to \rho\nu$ background are similar, their preselection efficiencies are similar.

Two additional isolation cuts were used, as these will help to reject QCD background events. The first one characterises the isolation of the track in the tracking detectors and the second one characterises the isolation of the calorimeter cluster in the calorimeters. An additional track is searched for inside a $\Delta R = 0.3$ cone centred on the track direction. Events were rejected if this extra track had transverse momentum larger than 2 GeV. Additional energy measured in the same cone in the calorimeter was required to be less than 3 GeV.

Table 5-8 shows the selection efficiency and the numbers of events expected for the relevant τ decay modes and for 10 fb^{-1} of integrated luminosity: 389 000 signal events and 138 000 background events from τ decays with neutral pions remain.

5.4.3.3 Results

The *E/p* ratio was studied for these events and is shown in Figure 5-40. The ratio is peaked at one for the signal process whereas the background ratio is shifted towards larger values, because of the energy deposited by neutral pions. At this level the residual bias of the global *E/p* distribution is 4%; the mean of the *E/p* is 1.039 for the full sample as can be seen from the figure. This must be reduced further if the calibration goal is to be met.

The fine granularity of the EM Calorimeter can be used to increase the rejection. A study of the distance in ΔR between the charged track and the photons (without any smearing and with E_T larger than 1 GeV) shows that 20% of the photons from π^0 decay are inside a cone, centred on the matching track, of $\Delta R = 0.025$ which is the size of a cell in the EM Calorimeter over the pseudorapidity range $|\eta| < 2.5$. By rejecting events where energy is observed *outside* this cone an additional rejection factor of order five might be obtained, re-

Figure 5-40 The distributions of *E/p* ratio for the signals (the dotted line, the mean value is 1.005, the rms is 0.140), the backgrounds (the dashed line, the mean value is 1.133, the rms is 0.239) and their sum (the solid line, the mean value is 1.039, the rms is 0.181) for integrated luminosity of 10 fb^{-1}.

ducing the residual bias in the *E/p* distribution below 1%. A study using full simulation is needed to assess this possibility as the shower spreading must be included.
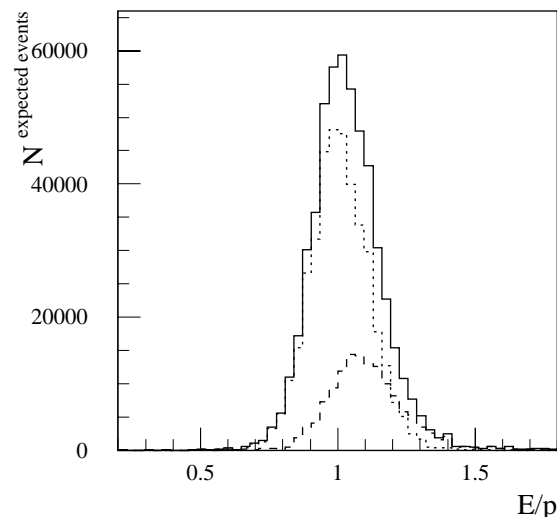
5.5 Conclusions

An extensive programme of beam tests of prototypes and module zero's of the hadronic calorimeters was carried out from 1994 to 1998. Beams of charged pions, electrons and muons were used to evaluate the performance of the calorimeters. These tests have been vital for optimising and finalising the design, structure, and read-out of the hadronic calorimeters.

These tests were accompanied by detailed studies, based on Monte Carlo simulation of the response of calorimeter modules to particles. These studies have considerably improved the understanding of the calorimeters. Comparison between experimental data, obtained in beam tests, and Monte Carlo predictions was used to verify the different hadronic shower models, used in simulations.

At the same time, the response of the whole ATLAS calorimeter system to single pions and muons was investigated using full simulation. In contrast to hadronic jets, analysis of the single particle data gives a clearer picture of the calorimeter response and of the energy loss in the dead material and in the crack regions between different calorimeters. Monte Carlo studies of single-particle response can connect the energy region up to 400 GeV (verified by comparison with test beam data) and the TeV region, which will be explored at the LHC.

First results, obtained with fast simulation, have shown that it might be possible to use the precise measurements of the energy and momentum of single isolated charged hadrons to transfer the test beam calibrations to the actual detector and to constrain the absolute energy calibration of the hadronic calorimeters.

5.6 References

5-1   ATLAS Collaboration, Calorimeter Performance Technical Design Report, ATLAS TDR 1, CERN/LHCC 96-40 (1996).

5-2   ATLAS Collaboration, Liquid Argon Calorimeter Technical Design Report, ATLAS TDR 2, CERN/LHCC 96-41 (1996).

5-3   ATLAS Collaboration, Tile Calorimeter Technical Design Report, ATLAS TDR 3, CERN/LHCC 96-42 (1996).

5-4   E. Berger *et al.*, Nucl. Inst. Meth. **A387** (1996) 333.

5-5   M. Cobal e*t al.*, 'Analysis results of the April 1996 combined test of the LArgon and TILECAL barrel calorimeter prototypes', ATLAS Internal Note ATL-TILECAL-98-168 (1998).

5-6   T.A. Gabriel and C. Zeitnitz, Nucl. Inst. Meth. **A349** (1994) 106.

5-7   R. Wigmans, Nucl.Instr. Meth. **A259** (1987) 389.

5-8   M.P. Casado and M. Cavalli-Sforza, 'H1-inspired analysis of the 1994 combined test of the Liquid Argon and Tilecal calorimeter prototypes', ATLAS Internal Note ATL-TILECAL-96-075 (1996).

5-9   I. Efthymiopoulos, 'Comparison between the ATLAS/TileCal hadron barrel calorimeter prototype test beam data and Hadronic Simulation packages', ATLAS Internal Note ATL-TILECAL-96-092 (1996); Frascati Physics Series Vol. VI (pp.497-507), VI Int.Conf. on Calorimetry in HEP, Frascati, June 8-14,1996.

5-10   M. Cobal and S. Nemecek, 'Electron Resolution with Tilecal Module 0', ATLAS Internal Note ATL-COM-TILECAL-99-010 (1999).

5-11   T. Davidek and R. Leitner, 'Parametrisation of the Muon Response in the Tile Calorimeter', ATLAS Internal Note ATL-TILECAL-97-114 (1997).

5-12   M. Lefebvre and D. O'Neil, 'End-cap Hadronic Calorimeter Offline Testbeam Software: The hec_adc Package Version 3.6', ATLAS Internal Note ATL-LARG-99-002 (1999).

5-13   W.E. Cleland and E.G. Stern, Nucl. Inst. Meth. **A338** (1994) 467.

5-14   M. Dobbs, M. Lefebvre, D. O'Neil, 'Hadronic End-cap Modules Zero Pion and Electron Energy Scan Analysis from April 98 Testbeam Data', ATLAS Internal Note ATL-LARG-99-001 (1999).

5-15   A.A. Minaenko, 'Analysis of Test-Beam Data, Obtained with Module Zero of Hadron End-Cap Calorimeter', ATLAS Internal Note ATL-COM-LARG-99-009 (1999).

5-16   M.S. Levitsky, 'Analysis of Muon Test-beam Data, Obtained with the HEC Module Zero in April and August 1998', ATLAS Internal Note ATL-COM-LARG-99-010 (1999).

5-17   R. Brun *et al.*, 'GEANT3', CERN DD/EE/84-1 (1986).

5-18   M. Bosman, Y. Kulchitsky, M. Nessi, 'Charged pion energy reconstruction in the ATLAS Barrel Calorimeter', ATLAS Internal Note ATL-COM-TILECAL-99-011 (1999).

5-19   H. Plothow-Besch, 'First Study on the Absolute Energy Calibration of the ATLAS Hadron Calorimeters using Isolated Single Hadrons', ATLAS Internal Note ATL-PHYS-95-067 (1995).

5-20   C. Biscarat, 'Calibration of the hadronic calorimeter using E/p from single hadrons', ATLAS Internal Note ATL-COM-CAL-99-003 (1999).

5-21   F. Abe *et al.*, Phys. Rev. Lett. **68** (1992) 3398;
        J. Alitti *et al.*, Z. Phys. **C52** (1991) 209.

5-22   T. Sjostrand, Computer Phys. Comm. **82** (1994) 74.

5-23   S. Jadach, Z. Was, J.H. Kuehn, Computer Phys. Comm. **64** (1991) 275; 'TAUOLA - A library of Monte Carlo programs to simulate decays of polarized τ leptons', CERN-TH-5856-90 (1990).

5-24   E. Richter-Was, D. Froidevaux, L. Poggioli, 'ATLFAST 2.0 a fast simulation package for ATLAS', ATLAS Internal Note ATL-PHYS-98-131 (1998).